A&A 674, A187 (2023)
https://doi.org/10.1051/0004-6361/202245808

Astronomy & Astrophysics

Systematics of planetary ephemeris reference frames inferred from pulsar timing astrometry

N. Liu (刘牛)[1,2], Z. Zhu (朱紫)[1], J. Antoniadis[3,4], J.-C. Liu (刘佳成)[1], and H. Zhang (张鸿)[1]

[1] School of Astronomy and Space Science, Key Laboratory of Modern Astronomy and Astrophysics (Ministry of Education), Nanjing University, Nanjing 210023, PR China
e-mail: zhuzi@nju.edu.cn
[2] School of Earth Sciences and Engineering, Nanjing University, Nanjing 210023, PR China
[3] Institute of Astrophysics, Foundation for Research and Technology-Hellas, Voutes, 71110 Heraklion, Greece
e-mail: john@ia.forth.gr
[4] Max-Planck-Institut für Radioastronomie, Auf dem Hügel 69, 53121 Bonn, Germany

Received 28 December 2022 / Accepted 27 April 2023

ABSTRACT

Aims. This study aims to investigate the systematic errors in planetary ephemeris reference frames through pulsar timing observations.
Methods. We used the published data sets from several pulsar timing arrays and performed timing analyses for each pulsar using different planetary ephemerides retrieved from the Jet Propulsion Laboratory's Development Ephemeris (DE), Ephemeris of Planets and the Moon (EPM), and INPOP (Intégration Numérique Planétaire de l'Observatoire de Paris). Then, we compared the timing solutions and modeled the differences in position and proper motion by vector spherical harmonics of the first degree. The timing solutions were also compared with those determined by very long baseline interferometry (VLBI) astrometry.
Results. The orientation offsets between the latest editions of the DE, EPM, and INPOP series do not exceed 0.4 milliarcseconds (mas), while the relative spins between these ephemerides are less than 5 microarcseconds per year (μas yr^{-1}). We do not detect significant glides in either position or proper motion between these ephemerides. The orientation of the pulsar timing frames deviates from that of the VLBI frame from zero by approximately 0.4 mas when considering the formal uncertainty and possible systematics.
Conclusions. The orientation of current planetary ephemeris frames is as accurate as at least 0.4 mas, and the nonrotation is better than 5 μas yr^{-1}.

Key words. astrometry – ephemerides – reference systems – pulsars: general

1. Introduction

Modern numerical planetary ephemerides have been used for various purposes in deep space missions (e.g., Yang et al. 2022), fundamental physics (e.g., Pitjeva et al. 2021; Bernus et al. 2019, 2020, 2022), dark matter (e.g., Pitjeva & Pitjev 2013), and planetary science (e.g., Liu & Capitaine 2017; Fienga et al. 2020a,b; Yuan et al. 2021). There are three main ephemeris series, namely, Jet Propulsion Laboratory's (JPL) planetary and lunar ephemerides Development Ephemeris (DE; Park et al. 2021), Ephemeris of Planets and the Moon (EPM) from the Institute of Applied Astronomy of the Russian Academy of Sciences (Pitjeva et al. 2022), and INPOP (Intégration Numérique Planétaire de l'Observatoire de Paris) ephemeris from the IMCCE (Institut de mécanique céleste et de calcul des éphémérides) at the Paris Observatory (Fienga et al. 2022). These planetary ephemerides realize the International Celestial Reference System (ICRS; Feissel & Mignard 1998) in a dynamical sense and are aligned onto the International Celestial Reference Frame (ICRF; Charlot et al. 2020) with an accuracy of submilliarcsecond (mas) by very long baseline interferometry (VLBI) and very long baseline array (VLBA) observations of the planetary spacecraft. These observations mainly include tracking measurements of the MErcury Surface, Space ENvironment, GEochemistry, and Ranging (MESSENGER) spacecraft orbiting Mercury (Verma et al. 2014); the Venus Express (VEX) and *Magellan* spacecraft orbiting Venus (Folkner et al. 1993, 1994a,c); the Mars Global Surveyor, Mars Odyssey, and Mars Reconnaissance Orbiter spacecraft orbiting Mars (Park et al. 2015); the *Galileo* and *Juno* spacecraft orbiting Jupiter (Jones et al. 2021); and the *Cassini* spacecraft orbiting Saturn (Jones et al. 2011, 2015, 2020). The orbits of inner planets are tied to ICRF by VLBI measurements of Mars-orbiting spacecraft (Park et al. 2021).

Understanding the systematic errors of the planetary ephemerides is essential for their users. The largest uncertainty in planetary positions comes from the shortcomings in the dynamical modelings (Standish & Fienga 2002). There are at least two methods to determine the uncertainty of the planetary ephemerides (Fienga et al. 2009). The first is to compare the extrapolated positions of planets with the observations outside the fit interval of the ephemerides (e.g., Fienga et al. 2013). The second is to assess the internal agreements between ephemerides from the same series that are constructed by identical or similar dynamical models (e.g., Standish 1990b) or external agreements between the state-of-the-art ephemerides from different series (e.g., Pitjeva 2005). These agreements are usually evaluated by comparing the heliocentric or geocentric coordinates of planets such as Earth or Mars (e.g., Tkachuk & Choliy 2013; Deng et al. 2014).

The pulsar timing technique precisely records the pulse times of arrival (TOAs) of pulsars, from which information about the

astrometry, rotation, and orbital motion can be inferred. One of the main objectives of pulsar timing astrometry is to search for nanohertz (nHz) gravitational wave signals in the timing observations of an ensemble of pulsars forming a pulsar timing array (PTA; Burke-Spolaor et al. 2019). The planetary ephemerides are used to compute the theoretical TOAs. It has been noted for a long time that the pulsar timing positions obtained by using different planetary ephemerides in the pulsar timing analysis vary, for instance, as found in Kaspi et al. (1994). Several authors reported that using updated versions of planetary ephemerides yielded an improved solution, leading to a more accurate measurement of astrometric parameters such as the parallax (Splaver et al. 2005; Hotan et al. 2006; Verbiest et al. 2008). As the precision of the timing astrometry is continuously improved to the level of a few tens of microarcseconds (μas), the systematic error in the planetary ephemerides is recognized as one of the main error sources that may degrade the sensitivity of the detection of gravitational waves (e.g., Chen et al. 2021).

Pulsar timing astrometry can also contribute to the investigation of systematics in planetary ephemerides with the advantage that pulsar timing observations are fully independent of the creation process of the planetary ephemerides. The signal in the residual of TOAs due to the systematics in the planetary ephemerides, such as the uncertainties in the orbits of outer planets, can be modeled in the timing analysis (Caballero et al. 2018; Vallisneri et al. 2020). The comparison of pulsar positions determined from VLBI and pulsar timing observations provides a direct tie between the planetary frames and the extragalactic frames (Bartel et al. 1996; Wang et al. 2017; Liu et al. 2023). It is also possible to compare different ephemerides via pulsar timing astrometry to provide an independent check on the external agreements between planetary ephemerides, as done in Fienga et al. (2011).

In this paper, we extend the related work of Fienga et al. (2011) by using recent data releases from several PTA data sets with increased sample sizes and improved astrometric precision and accuracy (Sect. 2.2), updated VLBI solutions of pulsars (Sect. 2.3), as well as modeling using the vector spherical harmonics (VSH; Mignard & Klioner 2012) of the ephemeris systematics (Sect. 2.4). Three motivations drive us to perform this study: (i) to investigate the realistic accuracy of current planetary ephemeris frames, (ii) to provide a transformation relation between planetary ephemerides, especially those produced by different groups, and (iii) to evaluate the implication of using different planetary ephemerides in the timing solutions on the derived astrometric parameters for pulsars. For these purposes, we compare the timing solutions based on the same sets of timing observations using different ephemerides (Sect. 3.1) and compare the timing solutions with the latest VLBI astrometric solutions (Sect. 3.3). Throughout the paper, the planetary ephemeris reference frame is referred to as the reference frame based on Earth's orbit provided by a given planetary ephemeris. The formal uncertainties (including the error bars) are always provided at a confidence level of 68%. The name of pulsars is given by their J2000 coordinates.

2. Materials and methods

2.1. Numerical planetary ephemerides

We downloaded the successive editions of the planetary ephemerides from the DE series[1], the EPM series[2], and the INPOP series[3]. Only the planetary ephemerides that worked properly with the timing analysis software were included in this work. We only considered the JPL DE ephemerides since DE403 because they were aligned onto the extragalactic reference frame, except for DE200, which was constructed on its own dynamical reference frame of J2000 (Standish 1982). This ephemeris was considered because it was intensively used in the previous timing analyses. For many pulsars (especially young, nonrecycled pulsars), the most recent timing solutions were given under the DE200 frame. Including DE200 in the comparison can thus provide a convenient transformation relation from these timing astrometric solutions referred to the DE200 frame to those referred to more recent planetary ephemerides. Only these DE ephemerides for a general purpose were considered, that is, DE200, DE405, DE421, DE430, and DE440, except for DE410, which was used for comparison with previous results (Sect. 4.1.1). The EPM series contained EPM2011, EPM2015, EPM2017, and EPM2021. For the INPOP series, we considered the latest version of each generation, which are INPOP06c, INPOP08a, INPOP10e, INPOP13c, INPOP17a, INPOP19a, and INPOP21a. In addition, INPOP10a and INPOP10b were included to illustrate the influence of different factors on the planetary ephemeris frames (Sect. 4.2). In total, we considered six DE ephemerides, four EPM ephemerides, and nine INPOP ephemerides.

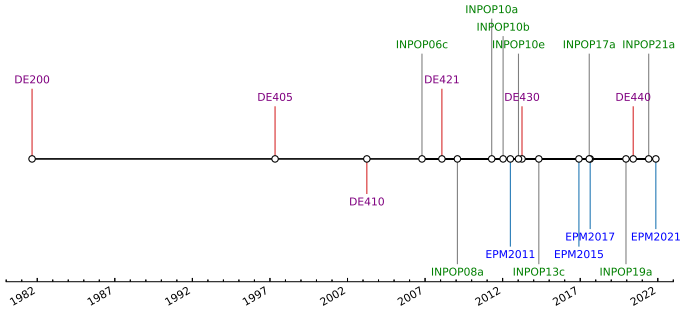

Fig. 1. Release timeline of the planetary ephemerides of the DE, EPM, and INPOP series. The release time is chosen to be the relevant date found in the online documents or publications accompanied by each ephemeris and may not be rigorously correct.

Figure 1 shows a rough timeline of the release dates of the ephemerides. One can expect that the ephemerides created at similar times may have comparable precision and accuracy, which has been validated in previous studies (e.g., Fienga et al. 2008). Table 1 lists the major differences in the VLBI observations of Mars spacecraft and asteroid perturbation modeling of the main belt objects and Kuiper belt objects between planetary ephemerides. These differences are supposed to be the most relevant to the differences between planetary ephemerides and the alignment accuracy of their frame axes onto ICRF, which are of interest in this work.

2.2. Pulsar timing data sets

We retrieved the pulsar timing data sets from several pulsar timing arrays, including data release 1.0 of the European Pulsar Timing Array (EPTA DR1; Desvignes et al. 2016), the extended second data release of the Parkes Pulsar Timing Array (PPTA DR2e; Reardon et al. 2021), the narrowband and wideband versions of the 12.5 yr data set of the North American Nanohertz Observatory for Gravitational Waves (NANOGrav12.5-NB and

[1] https://ssd.jpl.nasa.gov/planets/eph_export.html
[2] https://iaaras.ru/en/dept/ephemeris/epm/
[3] https://www.imcce.fr/recherche/equipes/asd/inpop/

Table 1. VLBI measurements of Mars spacecraft and asteroid modeling used for each planetary ephemeris considered in this work.

Ephemeris	VLBI observations of Mars			Dynamical modeling		Ref
	Period	Number	Accuracy (mas)	Main belt	Kuiper belt	
DE200	...	...	...	3	...	1
DE405	1989	2	10–100	300	...	2
DE410	1989–2003	33	0.5	300	...	3
DE421	2001–2007	94	<0.5	343	...	4–5
DE430	2001–2013	151	<0.2	343	...	6
DE440	2001–2020	316	0.18–0.25	343	30 + 1 ring	7
EPM2011	1989–2010	144	0.8	301 + 1 ring	21 + 1 ring	8
EPM2015	1989–2013	204	0.18–6.2	301 + 1 ring	30 + 1 ring	9
EPM2017	1989–2014	204	0.18–6.2	301 + 3 rings	30 + 3 rings	10
EPM2021	1989–2014	204	0.18–6.2	277 + 3 rings	30 + 3 rings	11
INPOP06c	1989–2003	44	0.5	300 + 1 ring	...	12
INPOP08a	1989–2007	96	0.4	303 + 1 ring	...	13
INPOP10a	1989–2007	96	0.4	161 + 1 ring	...	14
INPOP10b	1989–2007	96	0.4	161 + 1 ring	...	15
INPOP10e	1989–2007	96	0.4	161 + 1 ring	...	16
INPOP13c	1989–2007	96	0.4	139	...	17
INPOP17a	1989–2013	194	0.3	168	...	18
INPOP19a	1989–2013	194	0.3	343	3 rings	19
INPOP21a	1989–2013	194	0.3	343	500	20

Notes. The accuracy of the VLBI observations is given by a priori accuracy or the scatter (root-mean-squared or standard deviation) of postfit residuals in the literature.

References. (1) Standish (1990a); (2) Standish (1998); (3) Standish (2003); (4) Folkner et al. (2007); (5) Folkner et al. (2009); (6) Folkner et al. (2014b); (7) Park et al. (2021); (8) Pitjeva (2013); (9) Pitjeva (2017); (10) Pitjeva & Pitjev (2018); (11) Pitjeva et al. (2022); (12) Fienga et al. (2008); (13) Fienga et al. (2009); (14) Fienga et al. (2011); (15) Fienga et al. (2012); (16) Fienga et al. (2013); (17) Fienga et al. (2014); (18) Viswanathan et al. (2017); (19) Fienga et al. (2019); (20) Fienga et al. (2021).

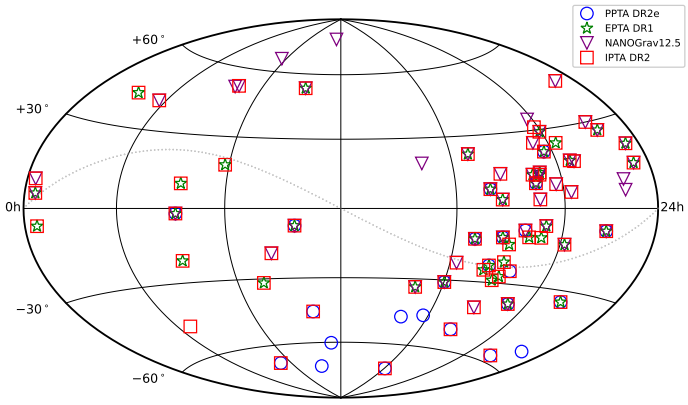

Fig. 2. Sky distribution of the pulsars contained in different PTA data sets in the equatorial coordinate system. The dotted curve indicates the location of the ecliptic plane.

NANOGrav12.5-WB; Alam et al. 2021a,b), and two versions (A and B) of the second data release of the International Pulsar Timing Array (IPTA DR2A and IPTA DR2B; Perera et al. 2019). All of these timing observations were made between 1986 and 2018. While the data set in the EPTA DR1, PPTA DR2e, and NANOGrav12.5 are obtained from independent observations of three regional PTAs in Europe, North America, and Australia, the IPTA combines the data sets from these individual PTAs to improve the sensitivity. The combination also leads to an increasing number of pulsars and better sky coverage compared to individual PTAs. For IPTA DR2, the input TOAs came from the previous data releases of these PTAs, which are EPTA DR1, the 9 yr data set from NANOGrav (Matthews et al. 2016), and the first data release of PPTA and its extended version (Reardon et al. 2016). The main difference between the two versions of IPTA DR2 (i.e., IPTA DR2A and IPTA DR2B) lies in the modeling of the dispersion measure and handling of the noise properties of pulsars. In this work, EPTA DR1, PPTA DR2e, and NANOGrav12.5 were used in addition to IPTA DR2 for two reasons. The first one was that PPTA DR2e and NANOGrav12.5 surpassed their previous data releases used to generate IPTA DR2 in terms of astrometric accuracy and sample size. There were five pulsars in PPTA DR2e and ten pulsars in NANAGrav12.5 that were not included in IPTA DR2. The other reason was that different PTAs with independent observations and analyses could be used to examine the consistency between results of planetary ephemeris comparison based on pulsar timing observations. The timing solutions from all the data sets were combined to derive the final results.

Since the planetary ephemerides are mainly constrained by observations on the ecliptic plane, it would be interesting to use only pulsars right on or close to the ecliptic plane. However, the major axis of the error ellipse tends to align with the ecliptic longitude for timing astrometry. The timing astrometric error ellipse would become extremely elongated for pulsars right on the ecliptic, making the measurement of right ascension and declination highly correlated and leading to a less reliable timing astrometric solution. One example in our sample is PSR J1022+1001, whose position is usually provided in the ecliptic coordinate system in the timing solution. We failed to reproduce timing solutions using several planetary ephemerides for this pulsar. This

Table 2. Astrometric precision of the timing solutions based on different PTA data sets using DE440.

PTA	Subset	Pos. Epoch	Nb. PSR	σ_{α^*} (μas)	σ_δ (μas)	$\sigma_{\mu_{\alpha^*}}$ (μas yr^{-1})	σ_{μ_δ} (μas yr^{-1})
PPTA DR2e	All	2011.8	24	47	89	12	22
	$\lvert\beta\rvert \le 10°$	2011.3	4	101	1469	29	427
	$\lvert\beta\rvert > 10°$	2012.0	20	40	74	9	16
EPTA DR1	All	2009.5	42	158	359	69	165
	$\lvert\beta\rvert \le 10°$	2009.5	12	197	2255	120	1046
	$\lvert\beta\rvert > 10°$	2009.5	30	140	302	67	136
NANOGrav12.5-WB	All	2013.6	47	82	156	44	89
	$\lvert\beta\rvert \le 10°$	2012.5	6	212	977	84	245
	$\lvert\beta\rvert > 10°$	2013.8	41	65	140	39	80
NANOGrav12.5-NB	All	2013.6	47	58	127	38	79
	$\lvert\beta\rvert \le 10°$	2012.4	6	230	996	82	247
	$\lvert\beta\rvert > 10°$	2013.8	41	58	108	30	58
IPTA DR2A	All	2010.2	64	161	320	60	154
	$\lvert\beta\rvert \le 10°$	2009.8	15	254	2171	119	924
	$\lvert\beta\rvert > 10°$	2010.3	49	147	248	45	77
IPTA DR2B	All	2010.2	64	145	314	59	136
	$\lvert\beta\rvert \le 10°$	2009.8	15	281	1763	140	977
	$\lvert\beta\rvert > 10°$	2010.3	49	109	173	44	70
Combination	All	2011.4	80	107	207	49	107
	$\lvert\beta\rvert \le 10°$	2010.4	15	240	1465	102	581
	$\lvert\beta\rvert > 10°$	2011.6	65	86	146	39	70

Notes. $\sigma_{\alpha^*} = \sigma_\alpha \cos\delta$ and $\sigma_{\mu_{\alpha^*}} = \sigma_{\mu_\alpha} \cos\delta$. The first four columns tabulate the PTA name, subset, mean position epoch, and the number of pulsars, followed by the typical precision (median) of the position and proper motion measurements. The last three rows represent the combination of all PTA data sets above.

pulsar might not be suitable for our analyses and thus was removed from our sample. We believe that missing one pulsar should not affect our results much because we studied the common features yielded in the timing solutions of all pulsars. To compare the results based on pulsars near or far from the ecliptic plane, we divided the sample into three subsets: all pulsars, pulsars close to the ecliptic plane (i.e., ecliptic latitude $|\beta| \le 10°$), and pulsars far from the ecliptic plane (i.e., $|\beta| > 10°$). Figure 2 depicts the sky distribution of all pulsars in the equatorial coordinate system, from which we found that the sample was dominated by pulsars at high ecliptic latitudes.

The timing models for each pulsar given in each PTA data set were directly used to rerun the timing analysis, except that different planetary ephemerides were adopted. We processed the published TOAs of all PTA data sets by `TEMPO2`[4] (version 2022.05.1; Hobbs et al. 2006). Noting that the planetary masses used in `TEMPO2` (defined as constant variables) usually differed from those used in the planetary ephemerides, we manually modified the values of the related variables in `TEMPO2` to be consistent with each planetary ephemeris to be studied. The timing astrometric solutions of all pulsars in each PTA under the same planetary ephemeris formed a pulsar catalog, which was considered as an independent representation of the reference frame of the used ephemerides.

Since the DE ephemerides were widely used in the pulsar timing analyses, we chose the timing solutions using DE440 as the reference solution for each PTA data set. Table 2 presents a brief overview of these reference solutions. The typical timing position precision (median) was approximately 50 μas–150 μas in right ascension and 100 μas–350 μas in declination. For the proper motion measurements, the typical precision was in the range of 10 μas yr^{-1} to 70 μas yr^{-1} in right ascension and twice as poor in declination. Comparing two samples of $|\beta| \le 10°$ and $|\beta| > 10°$, we found that the astrometric precision in either right ascension or declination for pulsars near the ecliptic plane was twice or more worse than those for pulsars away from the ecliptic plane, which is a typical feature of timing astrometry.

Assuming the timing precision merely consists of the measurement noise, the sensitivity to the systematics of the ephemeris frames to be examined would be improved by a factor of the root square of the number of pulsars in the sample. Using the values presented in Table 2, we obtained 8 μas to 24 μas for right ascension, 18 μas to 55 μas for declination, 2 μas yr^{-1} to 11 μas yr^{-1} for proper motion in right ascension, and 4 μas yr^{-1} to 26 μas yr^{-1} for proper motion in declination. The detection sensitivity in the position system was thus well below the orientation accuracy of the planetary ephemeris reference frames (i.e., ∼0.25 mas), enabling us to perform meaningful investigations into the possible systematics in the planetary ephemeris reference frames.

2.3. VLBI solutions of pulsars

We found the VLBI astrometric solutions for seven pulsars in our sample (PSR J1022+1001 excluded), which mostly came from the PSRπ and MSPSRπ campaigns (Deller et al. 2019). These sources were all included in the IPTA DR2 sample. Among these seven pulsars, six sources were common to the EPTA DR1 and NANOGrav samples, and two pulsars were found in PPTA DR2e. There are two pulsars with $|\beta| \le 10°$, which are PSR J2010−1323 and PSR J2145−0750.

[4] https://bitbucket.org/psrsoft/tempo2/src/master/

Table 3. Overview of timing and VLBI solutions for seven pulsars used for evaluating the rotation between the planetary ephemeris frames and the extragalactic frame.

Pulsar	Timing					VLBI					Ref.
	Epoch	σ_{α^*}	σ_δ	$\sigma_{\mu_{\alpha^*}}$	σ_{μ_δ}	Eopch	σ_{α^*}	σ_δ	$\sigma_{\mu_{\alpha^*}}$	σ_{μ_δ}	
		(μas)	(μas)	(μas yr^{-1})	(μas yr^{-1})		(μas)	(μas)	(μas yr^{-1})	(μas yr^{-1})	
J0437−4715	2009.5	5	5	1	2	2007.0	1015	994	50	90	1
J1012+5307	2009.5	49	64	10	14	2016.9	900	1000	90	140	2
J1640+2224	2009.5	46	65	13	19	2016.3	971	1000	80	140	3
J1713+0747	2009.5	5	10	1	2	2002.0	1486	2000	170	160	4
J2010−1323	2009.5	148	614	56	237	2012.2	1459	4000	329	303	5
J2145−0750	2009.5	97	268	25	69	2012.2	1486	4000	52	90	5
J2317+1439	2009.5	88	173	25	49	2012.2	1451	1000	465	704	5

Notes. The timing solutions were obtained through a timing analysis of the IPTA DR2B data set using DE440. The last column gives the reference to the VLBI position.

References. (1) Deller et al. (2009); (2) Ding et al. (2020); (3) Vigeland et al. (2018); (4) Chatterjee et al. (2009); (5) Deller et al. (2019).

We noted that the positional uncertainty in Deller et al. (2009) did not include the systematics due to the calibrator position uncertainty, core shift, and phase referencing errors from the primary calibrator to the in-beam calibrator. Therefore, we inflated the positional uncertainty therein using the same method as described in Liu et al. (2023). That is, we added in quadrature to the positional uncertainty given in Deller et al. (2009) an empirical value of 0.8 mas in each coordinate for the core-shift, 1.26 mas in right ascension and 0.59 mas in declination accounting for the phase referencing error, and the error in the absolute position of the calibrator. The positional precision of the timing and VLBI astrometric solutions is displayed in Table 3. The VLBI positional uncertainty now reaches ∼1 mas, while the timing positional uncertainty is at least ten times smaller. The correlations between right ascension and declination in the VLBI solutions were not available and were assumed to be zero.

The *Gaia* data also provided the astrometric solutions for pulsars in the *Gaia* reference frame (*Gaia*-CRF3; Gaia Collaboration 2022). We followed the method given in Antoniadis (2021) to search for pulsars in *Gaia* Data Release 3 (Gaia Collaboration 2023). We only found two pulsars, preventing us from performing a robust comparison between the planetary ephemeris frames and the *Gaia* reference frame.

2.4. Modeling of systematic differences in position and proper motion

The pulsar timing position and proper motion differences between using different planetary ephemerides and using DE440 were computed as

$$\Delta\alpha^* = (\alpha_\mathrm{e} - \alpha_\mathrm{r})\cos\delta_\mathrm{r}, \tag{1}$$
$$\Delta\delta = \delta_\mathrm{e} - \delta_\mathrm{r}, \tag{2}$$
$$\Delta\mu_{\alpha^*} = \mu_{\alpha^*,\mathrm{e}} - \mu_{\alpha^*,\mathrm{r}}, \tag{3}$$
$$\Delta\mu_\delta = \mu_{\delta,\mathrm{e}} - \mu_{\delta,\mathrm{r}}, \tag{4}$$

where the subscripts (as well as superscripts shown below) "r" and "e" represent the reference solution using DE440 and the timing solutions using planetary ephemerides other than DE440, respectively. The notation $\mu_{\alpha^*} = \mu_\alpha \cos\delta$, together with other similar notations (e.g., $\sigma_{\alpha^*} = \sigma_\alpha \cos\delta$), was used throughout the paper. We used the four-dimensional vector in the form of

$$\boldsymbol{y} = (\Delta\alpha^*,\ \Delta\delta,\ \Delta\mu_{\alpha^*},\ \Delta\mu_\delta)^\mathrm{T} \tag{5}$$

as the input observable. The full covariance matrix of the observable was expressed as

$$\boldsymbol{C_y} = \begin{bmatrix} \sigma^2_{\Delta\alpha^*} & C_{\Delta\alpha^*,\Delta\delta} & C_{\Delta\alpha^*,\Delta\mu_{\alpha^*}} & C_{\Delta\alpha^*,\Delta\mu_\delta} \\ C_{\Delta\alpha^*,\Delta\delta} & \sigma^2_{\Delta\delta} & C_{\Delta\delta,\Delta\mu_{\alpha^*}} & C_{\Delta\delta,\Delta\mu_\delta} \\ C_{\Delta\alpha^*,\Delta\mu_{\alpha^*}} & C_{\Delta\delta,\Delta\mu_{\alpha^*}} & \sigma^2_{\Delta\mu_{\alpha^*}} & C_{\Delta\mu_{\alpha^*},\Delta\mu_\delta} \\ C_{\Delta\alpha^*,\Delta\mu_\delta} & C_{\Delta\delta,\Delta\mu_\delta} & C_{\Delta\mu_{\alpha^*},\Delta\mu_\delta} & \sigma^2_{\Delta\mu_\delta} \end{bmatrix}, \tag{6}$$

where

$$\sigma_{\Delta\alpha^*} = \sqrt{\sigma^2_{\alpha^*,\mathrm{e}} + \sigma^2_{\alpha^*,\mathrm{r}}}, \tag{7}$$
$$\sigma_{\Delta\delta} = \sqrt{\sigma^2_{\delta,\mathrm{e}} + \sigma^2_{\delta,\mathrm{r}}}, \tag{8}$$
$$\sigma_{\Delta\mu_{\alpha^*}} = \sqrt{\sigma^2_{\mu_{\alpha^*},\mathrm{e}} + \sigma^2_{\mu_{\alpha^*},\mathrm{r}}}, \tag{9}$$
$$\sigma_{\Delta\mu_\delta} = \sqrt{\sigma^2_{\mu_\delta,\mathrm{e}} + \sigma^2_{\mu_\delta,\mathrm{r}}}, \tag{10}$$
$$C_{\Delta\alpha^*,\Delta\delta} = \rho^\mathrm{e}_{\alpha,\delta}\sigma_{\alpha^*,\mathrm{e}}\sigma_{\delta,\mathrm{e}} + \rho^\mathrm{r}_{\alpha,\delta}\sigma_{\alpha^*,\mathrm{r}}\sigma_{\delta,\mathrm{r}}, \tag{11}$$
$$C_{\Delta\alpha^*,\Delta\mu_{\alpha^*}} = \rho^\mathrm{e}_{\alpha,\mu_{\alpha^*}}\sigma_{\alpha^*,\mathrm{e}}\sigma_{\mu_{\alpha^*},\mathrm{e}} + \rho^\mathrm{r}_{\alpha,\mu_{\alpha^*}}\sigma_{\alpha^*,\mathrm{r}}\sigma_{\mu_{\alpha^*},\mathrm{r}}, \tag{12}$$
$$C_{\Delta\alpha^*,\Delta\mu_\delta} = \rho^\mathrm{e}_{\alpha,\mu_\delta}\sigma_{\alpha^*,\mathrm{e}}\sigma_{\mu_\delta,\mathrm{e}} + \rho^\mathrm{r}_{\alpha,\mu_\delta}\sigma_{\alpha^*,\mathrm{r}}\sigma_{\mu_\delta,\mathrm{r}}, \tag{13}$$
$$C_{\Delta\delta,\Delta\mu_{\alpha^*}} = \rho^\mathrm{e}_{\delta,\mu_{\alpha^*}}\sigma_{\delta,\mathrm{e}}\sigma_{\mu_{\alpha^*},\mathrm{e}} + \rho^\mathrm{r}_{\delta,\mu_{\alpha^*}}\sigma_{\delta,\mathrm{r}}\sigma_{\mu_{\alpha^*},\mathrm{r}}, \tag{14}$$
$$C_{\Delta\delta,\Delta\mu_\delta} = \rho^\mathrm{e}_{\delta,\mu_\delta}\sigma_{\delta,\mathrm{e}}\sigma_{\mu_\delta,\mathrm{e}} + \rho^\mathrm{r}_{\delta,\mu_\delta}\sigma_{\delta,\mathrm{r}}\sigma_{\mu_\delta,\mathrm{r}}, \tag{15}$$
$$C_{\Delta\mu_{\alpha^*},\Delta\mu_\delta} = \rho^\mathrm{e}_{\mu_{\alpha^*},\mu_\delta}\sigma_{\mu_{\alpha^*},\mathrm{e}}\sigma_{\mu_\delta,\mathrm{e}} + \rho^\mathrm{r}_{\mu_{\alpha^*},\mu_\delta}\sigma_{\mu_{\alpha^*},\mathrm{r}}\sigma_{\mu_\delta,\mathrm{r}}. \tag{16}$$

We used σ and ρ to represent the formal uncertainty and correlation coefficient, respectively. To quantify the significance of the position and proper motion difference, we adopted a normalized quantity $X_{\boldsymbol{y}}$ defined as

$$X^2_{\boldsymbol{y}} = \begin{bmatrix} \Delta\alpha^* & \Delta\delta & \Delta\mu_{\alpha^*} & \Delta\mu_\delta \end{bmatrix} \boldsymbol{C}^{-1}_{\boldsymbol{y}} \begin{bmatrix} \Delta\alpha^* \\ \Delta\delta \\ \Delta\mu_{\alpha^*} \\ \Delta\mu_\delta \end{bmatrix}. \tag{17}$$

We considered the global differences between both the position and proper motion systems of the planetary ephemerides, which would manifest themselves in the systematic changes of the pulsar timing positions and proper motions when different planetary ephemerides were used in the timing analyses. These global differences were modeled by the VSH of the first degree, including a rotation vector and a glide vector.

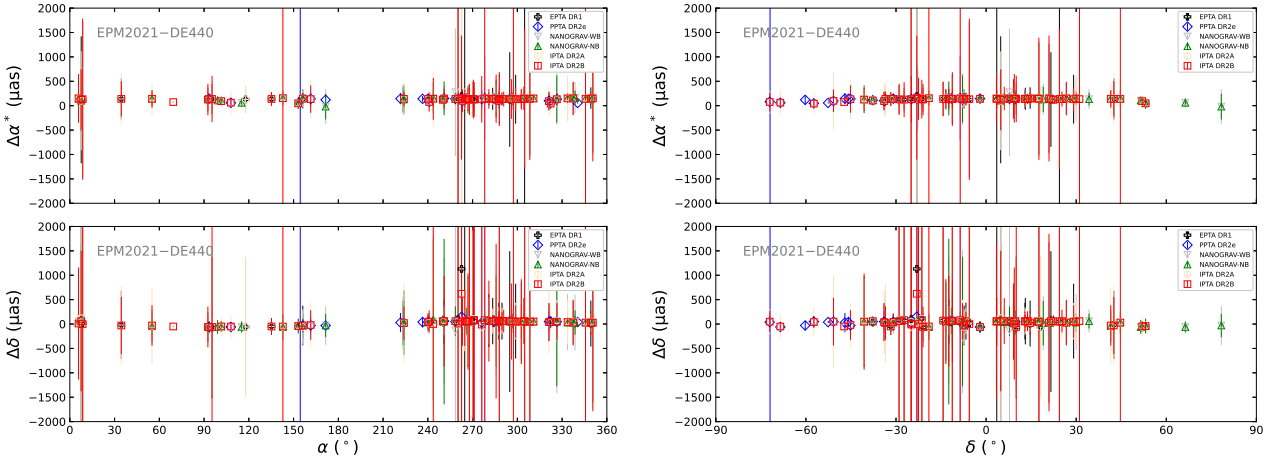

Fig. 3. Offsets of the pulsar timing positions in the EPM2021 frame with respect to those in the DE440 frame as a function of right ascension (left) and declination (right).

For the position system, the rotation vector $\boldsymbol{R} = (R_X, R_Y, R_Z)^T$ mainly represents the orientation offsets between the planetary ephemeris reference frames at the coordinate epoch t_0 (i.e., J2000). On the other hand, the glide vector $\boldsymbol{G} = (G_X, G_Y, G_Z)^T$ models a dipolar positional offset field that can be caused by the large-scale deformation in the planetary ephemeris reference frames and relative displacements and motions of the Solar System Barycenter (SSB) defined implicitly by the planetary ephemerides. The pulsar positional offsets at J2000 modeled by these two vectors can be expressed as

$$\begin{aligned}\Delta\alpha^*_0 = &- R_X \cos\alpha_r \sin\delta_r - R_Y \sin\alpha_r \sin\delta_r + R_Z \cos\delta_r \\ &- G_X \sin\alpha_r + G_Y \cos\alpha_r, \end{aligned} \tag{18}$$

$$\begin{aligned}\Delta\delta_0 = &+ R_X \sin\alpha_r - R_Y \cos\alpha_r \\ &- G_X \cos\alpha_r \sin\delta_r - G_Y \sin\alpha_r \sin\delta_r + G_Z \cos\delta_r. \end{aligned} \tag{19}$$

For the proper motion system, the rotation vector $\boldsymbol{r} = (r_X, r_Y, r_Z)^T$ characterizes the relative spin of the planetary ephemeris reference frames, which can be attributed to the mean motion difference in the orbital determinations of the Earth. Meanwhile, the glide vector $\boldsymbol{g} = (g_X, g_Y, g_Z)^T$ can be related to the relative accelerations of the SSB defined by different planetary ephemerides (if they exist). Similar to Eqs. (18)–(19), we obtained the pulsar proper motion offsets as

$$\begin{aligned}\Delta\mu_{\alpha^*,C} = &- r_X \cos\alpha_r \sin\delta_r - r_Y \sin\alpha_r \sin\delta_r + r_Z \cos\delta_r \\ &- g_X \sin\alpha_r + g_Y \cos\alpha_r, \end{aligned} \tag{20}$$

$$\begin{aligned}\Delta\mu_{\delta,C} = &+ r_X \sin\alpha_r - r_Y \cos\alpha_r \\ &- g_X \cos\alpha_r \sin\delta_r - g_Y \sin\alpha_r \sin\delta_r + g_Z \cos\delta_r. \end{aligned} \tag{21}$$

In addition, the resulting proper motion offsets can also lead to a positional displacement if the reference epoch t of the pulsar position differs from the coordinate epoch t_0 of the planetary ephemeris frame. Therefore, the total positional offsets due to the global differences of the aforementioned planetary ephemeris reference frame can be written as

$$\Delta\alpha^*_C = \Delta\alpha^*_0 + \Delta\mu_{\alpha^*,C}\,(t - t_0)\,, \tag{22}$$

$$\Delta\delta_C = \Delta\delta_0 + \Delta\mu_{\delta,C}\,(t - t_0)\,. \tag{23}$$

The VSH parameters (components in vectors $\boldsymbol{R}$, $\boldsymbol{G}$, $\boldsymbol{r}$, and $\boldsymbol{g}$) were determined by a least-squares fit of the model given by Eqs. (20)–(23) to the observables described by Eqs. (1)–(4). The observables were weighted by the inverse of the covariance matrix $\boldsymbol{C_y}$ given in Eq. (6). To improve the robustness of the fitting against the potential outliers, we computed the normalized difference X_y based on the postfit residuals following Eq. (17). The sources were considered outliers when the normalized differences exceeded the median value of the normalized differences for all sources by a chosen factor κ (called the clip limit), as used in Gaia Collaboration (2021). The fit was iterated until no new outlier was detected. We set $\kappa = 3$ in this work. Different values of κ were examined: the estimates of the VSH parameters changed little. We also adopted a bootstrap fit to cross-check the results of the least-squares fit. We generated 1000 trial samples, for which we randomly selected the same number of pulsars from the input sample with replacements. The least-squares fit was performed for each trial sample. The median value and the median absolute deviation (MAD) multiplied by a factor of 1.4826 (i.e., normalized MAD, which is equivalent to 1 σ in a Gaussian distribution) were used as the final estimate and the associated uncertainty for each unknown.

For the comparison between timing and VLBI astrometry, we first propagated the VLBI positions from their own epoch to those of the timing positions using the VLBI proper motions and then computed the offsets of the timing positions with respect to the propagated VLBI positions. The uncertainties of these positional offsets in either right ascension or declination were computed as the square root of the quadratic sum of both uncertainties in VLBI and timing positions as well as the propagation errors induced by the formal error in VLBI proper motion. Since there were a limited number of pulsars in common, we only modeled these offsets with the orientation offset, that is, the contribution from the vector $\boldsymbol{R}$, as given in Eqs. (18)–(19).

We performed the fit separately for each PTA data set to check their consistencies. The final estimates, together with their uncertainties, were obtained by a least-squares fit to the combination of the timing solutions from all PTAs.

3. Results

3.1. Offsets of the pulsar timing position and proper motion due to different ephemerides

Figures 3–4 depict the offsets of the timing positions derived using EPM2021 and INPOP21a with respect to those using DE440 at the original timing position reference epochs for each pulsar. The comparisons of the pulsar timing positions between other planetary ephemerides and DE440 are shown in

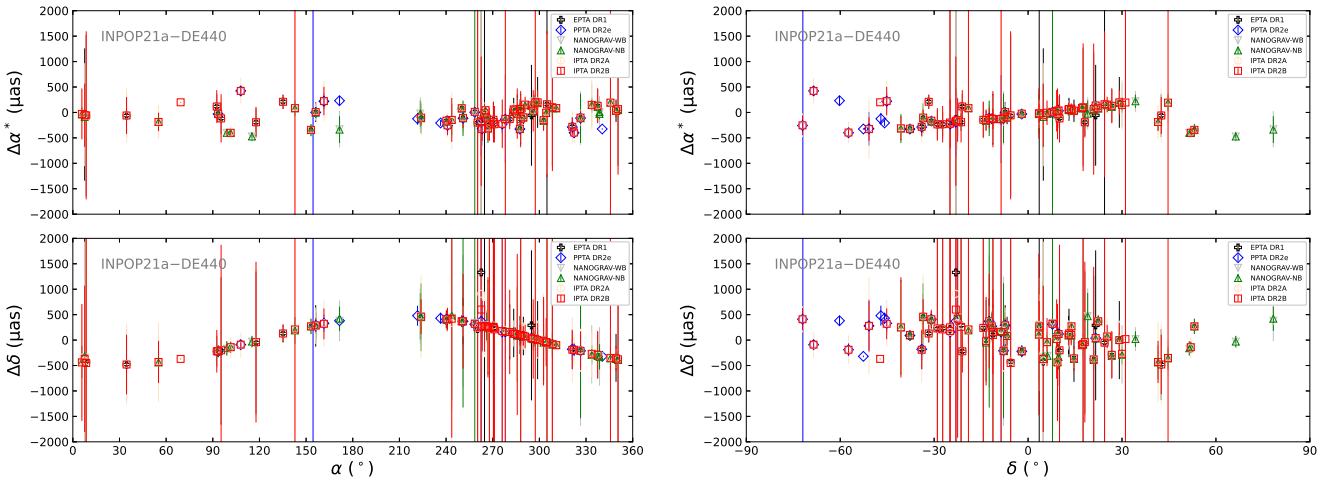

Fig. 4. Offsets of the pulsar timing positions in the INPOP21a frame with respect to those in the DE440 frame as a function of right ascension (left) and declination (right).

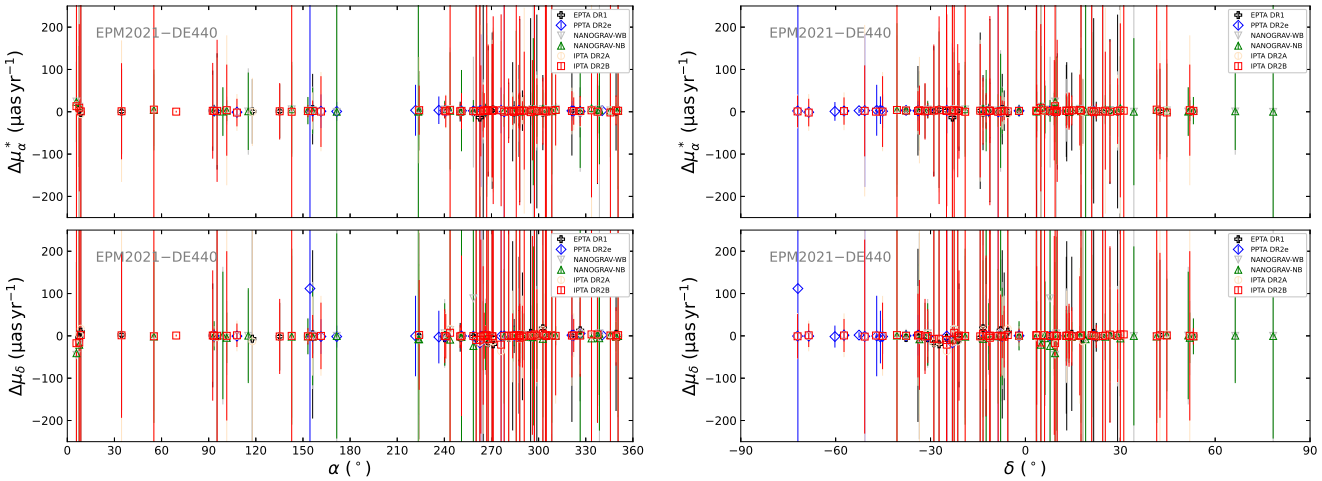

Fig. 5. Offsets of the pulsar timing proper motions in the EPM2021 frame with respect to those in the DE440 frame as a function of right ascension (left) and declination (right).

Appendix A. The differences in the right ascension are approximately 100 μas between EPM2021 and DE440 and 200 μas between INPOP21a and DE440, while the respective offsets in the declination are 50 μas and 300 μas. The weighted root-mean-squares (WRMS) in right ascension and declination are 118 μas and 55 μas for EPM2021 versus DE440 and 232 μas and 305 μas for INPOP21a versus DE440. These positional offsets are not significant over 1 σ compared to their uncertainties for approximately half of the pulsars. When using older planetary ephemerides, the positional offsets become more pronounced and significant; they are almost all confident at 1 σ for DE200 and DE405. In addition, we found obvious patterns in these plots, especially in the plots of $\Delta\alpha^*$ versus δ and $\Delta\delta$ versus α, which implied clear dependencies of the positional offsets on the right ascension and declination. The amplitude of these signatures exceeded the detection sensitivity of the PTA data sets mentioned in Sect. 2.2, suggesting that the global difference in the position system between planetary ephemerides could be determined with the timing solutions.

Similarly, the offsets of the pulsar timing proper motions using EPM2021 and INPOP21a with respect to those using DE440 are presented in Figs. 5–6, while the related plots for the remaining planetary ephemerides can be found in Appendix B. For most cases, we found a dominant proper motion bias in the right ascension, while the proper motion in the declination was much less affected. Except for a small fraction of pulsars, the differences in the proper motion in the right ascension are approximately 5 μas yr^{-1} for INPOP21a and EPM2021; they are only a few μas yr^{-1} in declination. These proper motion differences, however, are at least one order of magnitude smaller than their uncertainties and thus not statistically significant. We observed similar results between other planetary ephemerides and DE440, except those between DE200 and DE440 (Fig. B.1).

We also compared the timing astrometric solutions using the same ephemerides but based on different PTA data sets. These timing solutions based on the IPTA DR2B data set were used as the reference solutions. The positional agreements (WRMS) are between 30 μas and 60 μas in right ascension and between 60 μas and 180 μas in declination. For proper motion measurements, the agreements are ≤20 μas yr^{-1} for right ascension and between 20 μas yr^{-1} and 100 μas yr^{-1} for declination.

3.2. Modeling the differences

We modeled the pulsar timing position and proper motion offsets seen in the previous section following methods introduced in Sect. 2.4. The least-squares fits converged after two iterations or less. The WRMS of postfit residuals was reduced to a few μas

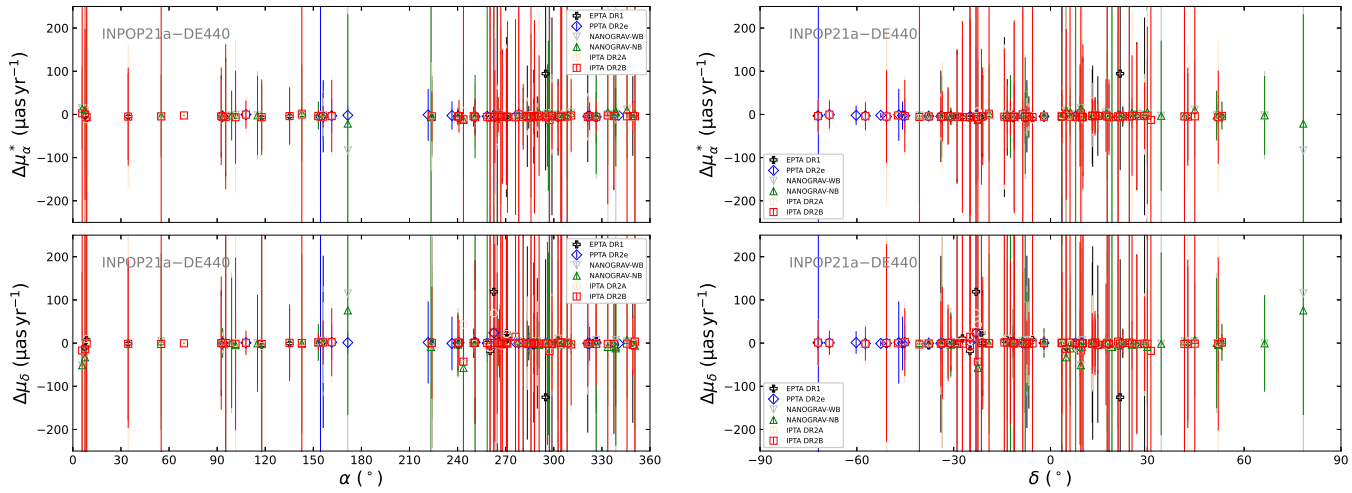

Fig. 6. Offsets of the pulsar timing proper motions in the INPOP21a frame with respect to those in the DE440 frame as a function of right ascension (left) and declination (right).

for the position and a few μas yr^{-1} for the proper motion. This suggested that the variations in the timing position and proper motion were well accounted for by our models.

However, we found a few large deviations from the bulk of the sample for a few pulsars (e.g., PSR J1730–2304 and PSR J1949+3106), for which the precision of the timing astrometric solutions was relatively low compared to the rest of the pulsars (approximately 10 mas for position and 5 mas yr^{-1} for proper motions). This implied that the systematics in the planetary ephemeris reference frames could be evinced in the pulsar timing data set only when the timing astrometric precision is sufficiently high.

The estimates of the VSH parameters based on various PTA data sets are depicted in Figs. 7–10, which show good agreement among different PTAs. We observed a general trend of declining to zero for the successive DE ephemerides, supporting a better global agreement between newer editions of the DE ephemerides. Similar results can be found for the successive EPM and INPOP ephemerides if one takes the results of the latest versions of each series (i.e., EPM2021 and INPOP21a) as the reference. The positional glide parameters (components in $\boldsymbol{G}$) were estimated to be 10 μas to 20 μas for most cases, obviously smaller than the corresponding positional rotation parameters (components in $\boldsymbol{R}$). This comment is also valid for the VSH parameters of the proper motion system. We also noticed that the X-component of the rotation vector $\boldsymbol{r}$ (∼1 μas yr^{-1}) is much less pronounced than the Y- and Z-components.

Table 4 presents estimates of the rotation and glide parameters of the position system among the planetary ephemerides based on the combination of the timing solutions from all PTAs. Except for earlier DE planetary ephemerides (DE200 and DE405), the orientation offsets were generally less than 500 μas, and almost no relative dipolar deformation was effectively detected.

We tabulated the determinations of the VSH parameters among the planetary ephemeris proper motion systems in Table 5. The spin around the X-axis is much smaller than those around the Y- and Z-axes. We converted the spin vectors from the equatorial coordinate system to the ecliptic coordinate system and found that the spins were mainly in the direction of the latitude, suggesting that the spin was likely due to the differences in the mean orbital motion of Earth. The glide parameters were less than 1 μas yr^{-1} and were statistically insignificant for most cases.

The VSH fittings were also applied to the subsets of pulsars at high and low ecliptic latitudes. The results of pulsars near the ecliptic plane showed some discrepancies compared to the results based on subsets of all pulsars and only pulsars far from the ecliptic plane, which usually occurred for parameters on the Z-axis. The most pronounced differences occurred for the comparison between DE200 and DE440, for which the sample of pulsars at low ecliptic latitudes yielded a solution of $G_Z = -634 \pm 375$ μas and $g_Z = 36 \pm 32$ μas yr^{-1}. These discrepancies, however, were not statistically significant with respect to the uncertainties of the estimates for most cases.

The bootstrap fit gave consistent results with those from the least-squares fit (i.e., reported in Tables 4 and 5), while the formal uncertainty was usually several times larger than the formal uncertainty of the latter. To cross-check the results, we processed the NANOGrav12.5 data set using `PINT`[5] (version 0.9.1; Luo et al. 2021) developed by the NANOGrav team under the DE planetary ephemeris frames, from which the results were consistent with those given by `TEMPO2`.

It was also possible to extend our VSH model to high degrees, for example, to degree two to include the quadrupolar terms. However, we noticed that the postfit WRMS in the timing positions and proper motions were already small. Including higher orders of VSHs might not improve the fit much. The quadrupolar signals, if they exist, should not exceed 5 μas in the positions and 1 μas yr^{-1} in the proper motions. Comparisons among timing solutions using DE440, EPM2021, and INPOP21a were used to test this speculation. The VSH model was extended to different maximum degrees $l_{\max}$ until $l_{\max} = 5$, to which the differences between timing solutions were fitted. We found that the estimates of the rotation and glide parameters varied slightly when $l_{\max} \leq 4$. Figure 11 shows the evolution of the WRMS of postfit residuals as $l_{\max}$ increases, which changes little compared to that of $l_{\max} = 1$. The results of this experiment suggest that the VSH model of the first degree is sufficient to account for the global differences in position and proper motions between planetary ephemerides.

3.3. Comparison between timing and VLBI solutions

The positional offsets between the timing and VLBI solutions are presented in Figs. 12–14. Only the results of timing solutions

[5] https://pypi.org/project/pint-pulsar/

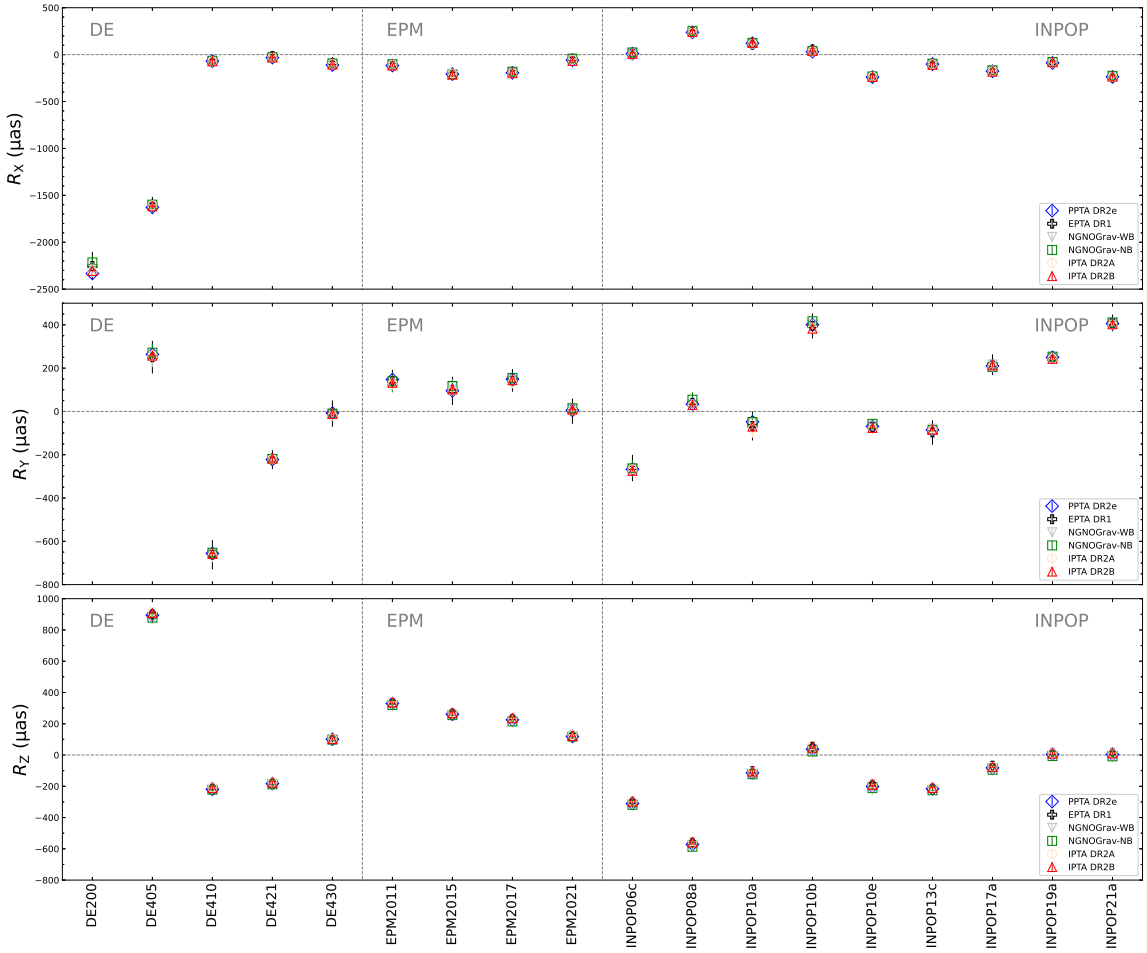

Fig. 7. Rotation parameters around the X-, Y-, and Z-axes in the position system of the planetary ephemeris frames with respect to DE440 in the equatorial coordinate system (from top to bottom). R_Z between DE200 and DE440 is approximately −12 mas, which is beyond the range of the vertical axis.

Table 4. Rotation and glide of the position system of planetary ephemerides with respect to that of DE440 in the equatorial coordinate system.

Ephemeris	R_X (μas)	R_Y (μas)	R_Z (μas)	G_X (μas)	G_Y (μas)	G_Z (μas)
DE200	−2291(22)	−12432(19)	−12428(13)	8(14)	−1(17)	−17(25)
DE403	−1838(13)	597(13)	−2309(8)	10(9)	−17(12)	−6(16)
DE405	−1623(13)	248(12)	891(9)	6(9)	−8(11)	−5(16)
DE410	−66(9)	−665(8)	−219(5)	2(5)	−1(7)	−1(11)
DE421	−33(7)	−227(7)	−184(4)	−2(3)	−3(5)	−0(8)
DE430	−106(7)	−14(7)	101(3)	1(3)	−1(6)	2(9)
EPM2011	−113(8)	132(8)	327(4)	−1(4)	−6(7)	2(9)
EPM2015	−204(8)	97(7)	258(5)	−2(5)	−2(7)	−1(10)
EPM2017	−192(8)	140(8)	223(4)	−1(4)	−4(7)	0(10)
EPM2021	−58(6)	8(6)	120(3)	1(3)	−1(5)	2(7)
INPOP06c	3(11)	−275(10)	−308(7)	1(8)	−3(10)	−5(13)
INPOP08a	244(9)	32(9)	−572(5)	2(4)	−6(7)	0(10)
INPOP10a	116(10)	−66(8)	−116(5)	−3(6)	6(9)	−9(12)
INPOP10b	38(12)	388(10)	29(7)	2(7)	−5(10)	1(16)
INPOP10e	−229(8)	−74(7)	−202(5)	0(5)	−5(6)	−1(10)
INPOP13c	−107(7)	−86(6)	−218(4)	−3(4)	1(6)	0(8)
INPOP17a	−176(9)	208(10)	−81(4)	1(4)	−4(7)	1(10)
INPOP19a	−83(6)	246(6)	4(3)	−2(3)	−2(5)	−1(7)
INPOP21a	−237(4)	405(5)	3(3)	−3(3)	−2(5)	2(6)

Notes. The uncertainties for the estimates given in parentheses were obtained from the least-squares fit and could be underestimated several times, as suggested by the bootstrap fit.

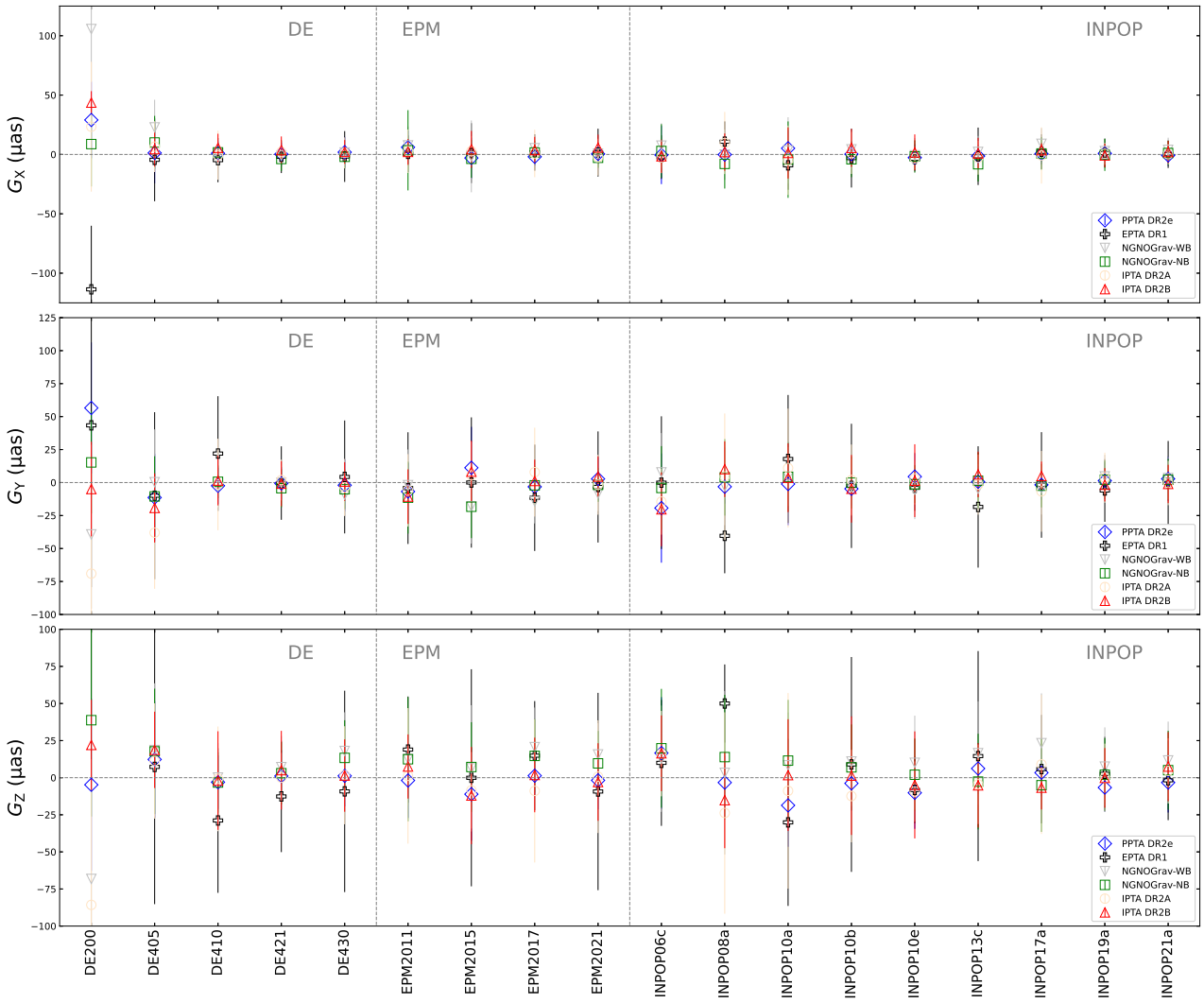

Fig. 8. Glide parameters around the X-, Y-, and Z-axes in the position system of the planetary ephemeris frames with respect to DE440 in the equatorial coordinate system (from top to bottom).

using DE200, DE405, and DE440 are shown here; the results of using other planetary ephemerides are similar to those of using DE440 and thus not plotted. The positional offsets between DE200 and VLBI reach −20 mas for some pulsars, while they decrease to approximately 4 mas or less between DE440 and VLBI, with uncertainties of 1 mas to 4 mas in either right ascension or declination. The results based on different PTA data sets are consistent within their astrometric precision.

The fittings of a frame rotation were performed to the positional offsets using each PTA data set separately except PPTA DR2e (due to the small sample size of pulsars in common) as well as their combination. The estimates of rotation parameters based on the IPTA DR2 data sets always differed by 0.3 mas to 0.6 mas from those based on the data sets from regional PTAs, although they still agreed with each other with their uncertainties returned by the least-squares fitting. These differences indicate possible systematics of the same level in the input VLBI and/or timing astrometric solutions.

Table 6 reports the fitting results based on the combination of all data sets. We found an orientation offset of ∼−3 mas on the X-axis and of <−10 mas on the Y- and Z-axes in the DE200 frame. We also detected an orientation offset of ∼−2.5 mas on the X-axis for the DE405 frame. The rest of the planetary ephemerides yield a common orientation offset of ∼−1.0 mas on the X-axis.

Since there were only two pulsars near the ecliptic plane, we could not use this subset to test the contribution of pulsars near the ecliptic plane to the determination of the frame rotation parameters. Instead, we excluded these two pulsars, leaving only pulsars with high ecliptic latitudes in the sample, and reran the solution. We found excellent agreements in the estimates of R_X and R_Y, while there was an offset of ∼−0.2 mas in the estimate of R_Z with respect to the solution using all pulsars. We speculated that this offset was caused by the removal of PSR J2145–0750, which yielded an offset of ∼+0.8 mas in right ascension between timing and VLBI. An increase in the sample size might lead to a more robust fit of the frame rotation.

4. Discussion

4.1. Comparison with previous results

4.1.1. Intercomparison among planetary ephemerides

Standish (2004a) compared DE200 and DE405 with DE409 (the newest edition of the DE series at that time) to approximate the

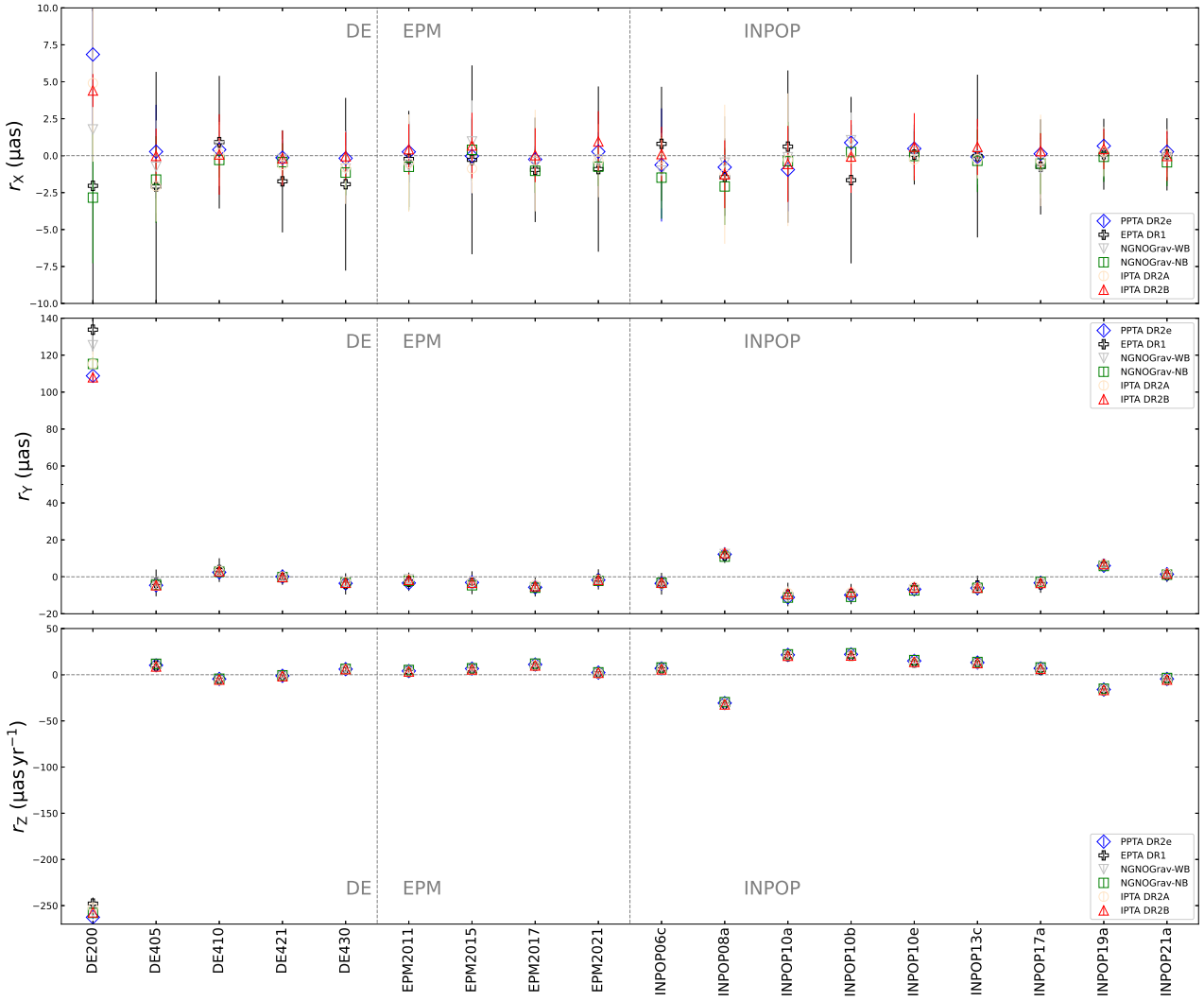

Fig. 9. Rotation parameters around the X-, Y-, and Z-axes in the proper motion system of the planetary ephemeris frames with respect to DE440 in the equatorial coordinate system (from top to bottom).

accuracy of DE200 and DE405. Based on the heliocentric coordinates of the Earth–Moon barycenter, the author gave the rotation relations between DE200 and DE409 and between DE405 and DE409 at J2000. The rotation relation can be rewritten as

$$\boldsymbol{R}_{\rm DE200} = \begin{bmatrix} -2200 \\ -11700 \\ -12300 \end{bmatrix} \mu{\rm as},\ \boldsymbol{r}_{\rm DE200} = \begin{bmatrix} +3 \\ +108 \\ -249 \end{bmatrix} \mu{\rm as\,yr}^{-1}, \quad (24)$$

for DE200 and

$$\boldsymbol{R}_{\rm DE405} = \begin{bmatrix} -1500 \\ +1000 \\ +1100 \end{bmatrix} \mu{\rm as},\ \boldsymbol{r}_{\rm DE405} = \begin{bmatrix} +1 \\ -7 \\ +15 \end{bmatrix} \mu{\rm as\,yr}^{-1}, \quad (25)$$

for DE405 by converting to the same units used in this work. We computed the relative orientation offsets and spins of DE200 and DE405 with respect to DE410 by comparing the rotation parameters for DE200 and DE405 with those for DE410 reported in Tables 4–5. Assuming that DE409 was very close to DE410, we obtained consistent results with those of Standish (2004a) given in Eqs. (24)–(25), which validated the effectiveness of our method. The relative spin found in the DE200 frame mainly reflects the mean motion errors of DE200 for the Earth–Moon barycenter (EMB), which was caused by the relatively short time-span coverage of the input ranging data used for deriving DE200 and the lack of asteroids in modeling their perturbations, as explained in Standish (2004a). The relative spin between DE405 and DE410 suggested a difference in the mean motion of Earth, as reported in Standish (2003), which was mainly caused by the differences in the modeling of perturbation from the largest 20 asteroids and more accurate fitting of Mars' orbit in DE410 compared to DE405.

Adopting a different computation of the asteroid perturbation compared to DE405 (considering perturbations of all 300 asteroids on all the planets and using an asteroid ring), the accuracy obtained with INPOP06 was improved to be comparable to the accuracy of DE414 (Fienga et al. 2008). We observe in Table 4 that the rotation and glide estimates for INPOP06c were much smaller than those of DE405 with respect to DE440. The accuracy of the Earth's orbit of DE421 was continuously improved by new VLBI tracking observations of spacecraft (Standish 2004b; Folkner et al. 2007, 2009). In addition, the asteroid perturbation was modeled as the effects of 67 asteroids with individual masses and 276 asteroids whose masses were defined by different density classes. These improvements were reflected in the smaller values of the rotation and glide parameters between DE421

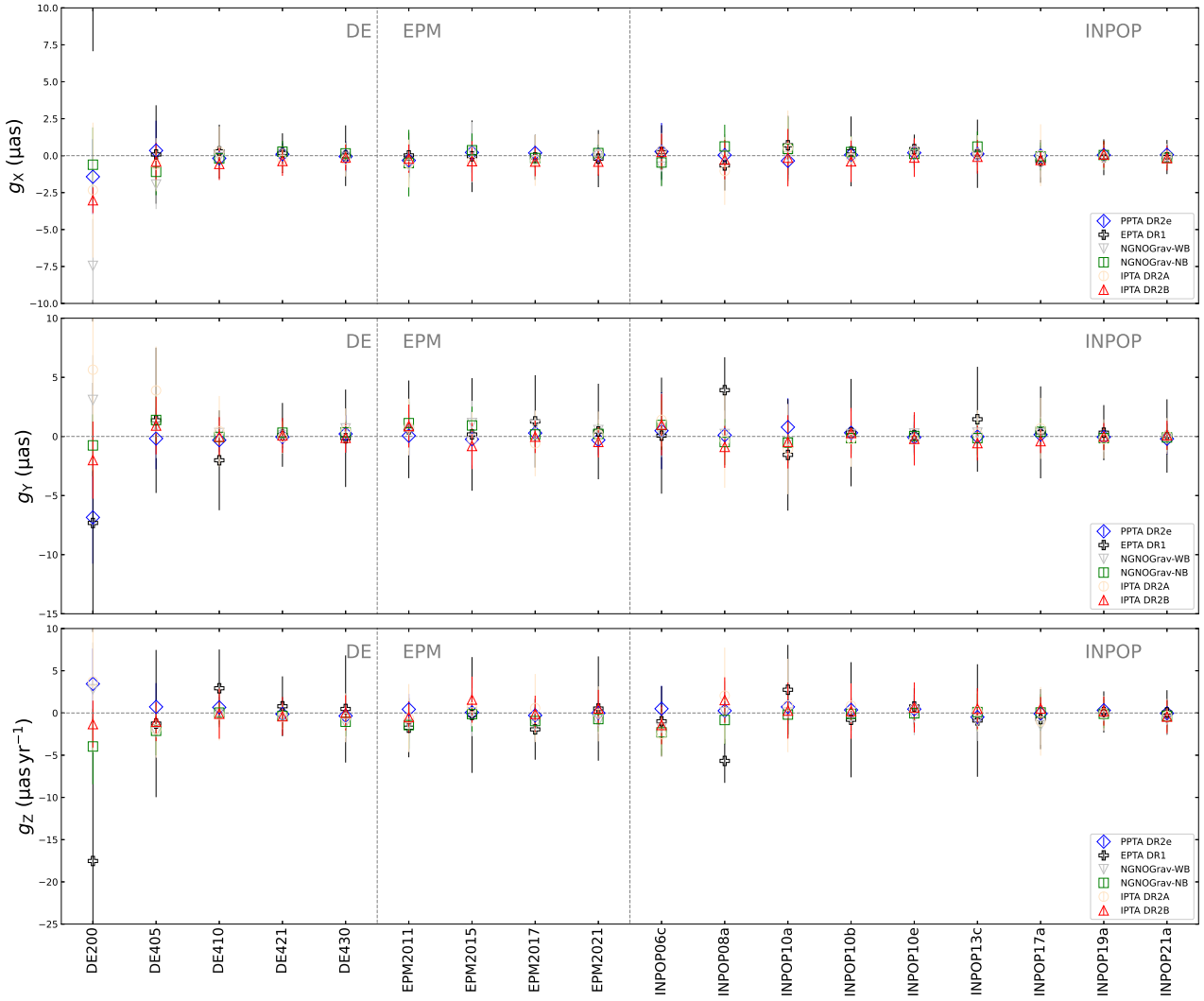

Fig. 10. Glide parameters around the X-, Y-, and Z-axes in the proper motion system of the planetary ephemeris frames with respect to DE440 in the equatorial coordinate system (from top to bottom).

and DE440 compared to those between DE410 and DE440. For INPOP08a, the ring model and asteroid selection were revised. Fienga et al. (2009) showed that the heliocentric longitudes of the EMB in the ecliptic coordinate computed using INPOP08 differed from those computed using DE421 or INPOP06 by a general linear drift, resulting in an ecliptic longitude offset of −3 mas over 100 yr. It corresponded roughly to a difference of $-30\,\mu\mathrm{as\,yr}^{-1}$ in the spin around the Z-axis in the ecliptic coordinate, which agreed with the spin reported in Table 5.

The main differences between INPOP08a and INPOP10a were the input data sets and the implementation of the fit. Fienga et al. (2011) used timing astrometric solutions of 18 millisecond pulsars with a precision of better than 10 mas to estimate the relative orientation offset between DE200, DE405, DE414, DE421, INPOP08, and INPOP10a. The reported results agreed with those obtained in this work within the formal uncertainties. Thanks to the increasing numbers of millisecond pulsars, more timing observations accumulated over more than 10 yr and from more radio telescopes, and improvements achieved in the timing observing system, our results were several times more precise than those in Fienga et al. (2011), reaching a precision of several tens of μas. EPM2011 was the first edition of the EPM series included in this work. Pitjeva (2013) reported that the maximum differences in the heliocentric positions of Mars between EPM2011 and DE424 were approximately 0.7 mas in right ascension and 0.5 mas in declination. Our fitting suggested that the frame rotation between EPM2011 and DE421 was approximately 0.4 mas around the Y-axis and 0.5 mas around the Z-axis.

No ring model accounting for the perturbation of the Main belt objects was considered in the INPOP series since INPOP13c. The comparison of the geocentric coordinates of Mars between INPOP13c and DE430 provided by Fienga et al. (2014) showed that the differences in right ascension and declination were all below 0.5 mas. In this work, the agreement in the orientation of each axis between INPOP13c and DE430 was found to be approximately 0.3 mas or better, which was thus consistent with the results in Fienga et al. (2014). The asteroid perturbation models were slightly modified in EPM2015 and EPM2017 compared to EPM2011. We found an orientation agreement of ∼0.1 mas among these planetary ephemeris reference frames. The dynamical modeling of INPOP17a was almost the same as that of INPOP13c. The differences in the heliocentric positions of Mars between INPOP17a and DE430 given by the comparison in Viswanathan et al. (2017) were approximately 0.2 mas in both right ascension and declination, close to the differences in the

Table 5. Rotation and glide of the proper motion system of planetary ephemerides with respect to that of DE440 in the equatorial coordinate system.

Ephemeris	r_X (μas yr^{-1})	r_Y (μas yr^{-1})	r_Z (μas yr^{-1})	g_X (μas yr^{-1})	g_Y (μas yr^{-1})	g_Z (μas yr^{-1})
DE200	2.4(1.6)	114.6(1.5)	−259.0(1.0)	−0.7(1.0)	0.4(1.3)	−0.3(1.9)
DE403	2.1(1.0)	−4.8(1.0)	20.1(0.6)	−1.0(0.7)	1.9(0.9)	−0.7(1.2)
DE405	−0.7(1.0)	−3.2(0.9)	10.8(0.7)	−0.8(0.7)	1.1(0.8)	−1.1(1.2)
DE410	−0.2(0.7)	3.5(0.6)	−4.7(0.4)	−0.2(0.4)	0.1(0.5)	−0.1(0.8)
DE421	−0.2(0.5)	0.3(0.5)	−1.0(0.3)	0.2(0.3)	0.3(0.4)	0.0(0.6)
DE430	−0.4(0.6)	−3.2(0.5)	6.1(0.3)	−0.1(0.3)	0.1(0.4)	−0.3(0.6)
EPM2011	−0.1(0.6)	−1.9(0.6)	4.3(0.3)	−0.0(0.3)	0.7(0.5)	−0.6(0.7)
EPM2015	0.0(0.6)	−3.3(0.6)	6.6(0.4)	0.2(0.4)	0.1(0.6)	0.3(0.8)
EPM2017	−0.5(0.6)	−5.1(0.6)	11.2(0.3)	0.1(0.3)	0.4(0.5)	−0.1(0.7)
EPM2021	0.0(0.5)	−1.9(0.5)	2.3(0.2)	0.0(0.3)	0.1(0.4)	−0.2(0.6)
INPOP06c	−0.5(0.8)	−2.7(0.8)	7.0(0.5)	−0.3(0.6)	0.7(0.7)	−0.9(1.0)
INPOP08a	−1.6(0.7)	12.3(0.6)	−30.9(0.4)	−0.1(0.3)	0.5(0.5)	−0.2(0.8)
INPOP10a	0.1(0.7)	−10.0(0.6)	21.5(0.4)	0.3(0.4)	−0.5(0.6)	1.0(0.9)
INPOP10b	0.3(0.9)	−9.0(0.7)	22.5(0.5)	−0.1(0.5)	0.4(0.7)	0.1(1.1)
INPOP10e	−0.1(0.6)	−6.1(0.5)	15.0(0.4)	−0.0(0.4)	0.4(0.5)	0.2(0.7)
INPOP13c	0.4(0.5)	−5.9(0.5)	13.3(0.3)	0.2(0.3)	−0.0(0.4)	0.1(0.6)
INPOP17a	−0.1(0.7)	−3.0(0.7)	6.8(0.3)	−0.0(0.3)	0.3(0.6)	−0.2(0.8)
INPOP19a	0.1(0.5)	6.5(0.5)	−16.0(0.3)	0.2(0.3)	0.1(0.4)	0.1(0.5)
INPOP21a	−0.0(0.3)	1.5(0.4)	−4.6(0.2)	0.2(0.2)	0.2(0.4)	−0.2(0.5)

Notes. The uncertainties for the estimate given in parentheses were obtained from the least-squares fit and could be underestimated several times, as suggested by the bootstrap fit.

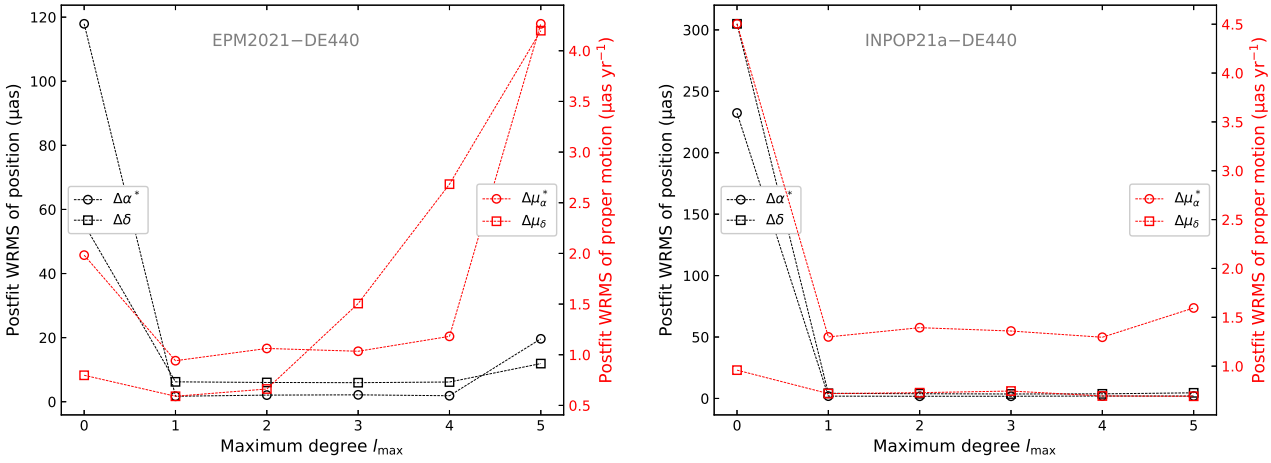

Fig. 11. WRMS of the postfit residuals as a function of the maximum degree of the VSH model. Left: EPM2021 versus DE440. Right: INPOP21a versus DE440.

rotation parameters between these two planetary ephemeris reference frames. A new model for the Trans-Neptunian objects was introduced in INPOP19a in addition to the increase in the amount of main-belt asteroids in comparison to INPOP17a, leading to a difference of ∼100 km in the barycentric position of the EMB that was mainly in the direction perpendicular to the ecliptic (Fienga et al. 2019). It seemed that, however, these improvements did not greatly affect the orientation of the INPOP reference frame. Fienga et al. (2021) compared the heliocentric position of Earth between DE440 and INPOP21a, which gave an agreement of 0.2 mas in right ascension and 0.4 mas in declination. These values agreed roughly with the orientation offset between DE440 and INPOP21a frames determined from the timing astrometry.

Comparisons with previous results based on other data sets or methods have validated the effectiveness of our method. Therefore, the transformation relation between other planetary ephemerides that are not included in this study might also be derived following the same procedure as described in Sect. 2.4.

4.1.2. Comparison between planetary ephemerides and extragalactic frames

DE200 was constructed on its own dynamical equinox of J2000.0 with an accuracy of 1 arcsecond (Standish 1982). Folkner et al. (1994b) estimated the orientation offset between the DE200 frame and extragalactic frame to be approximately −2 mas, −12 mas, and −6 mas around the X-, Y-, and Z-axes in 1988 by a joint analysis of the lunar laser ranging and VLBI measurements. These values roughly match our determination of the

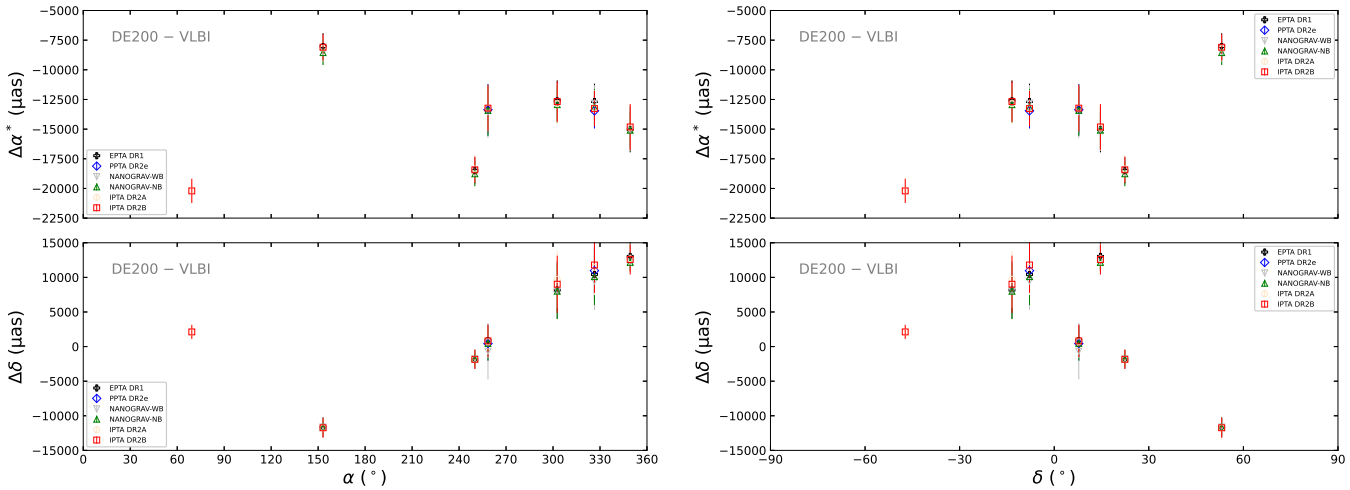

Fig. 12. Offsets of the pulsar timing positions in the DE200 frame with respect to those in the VLBI frame as a function of right ascension (left) and declination (right).

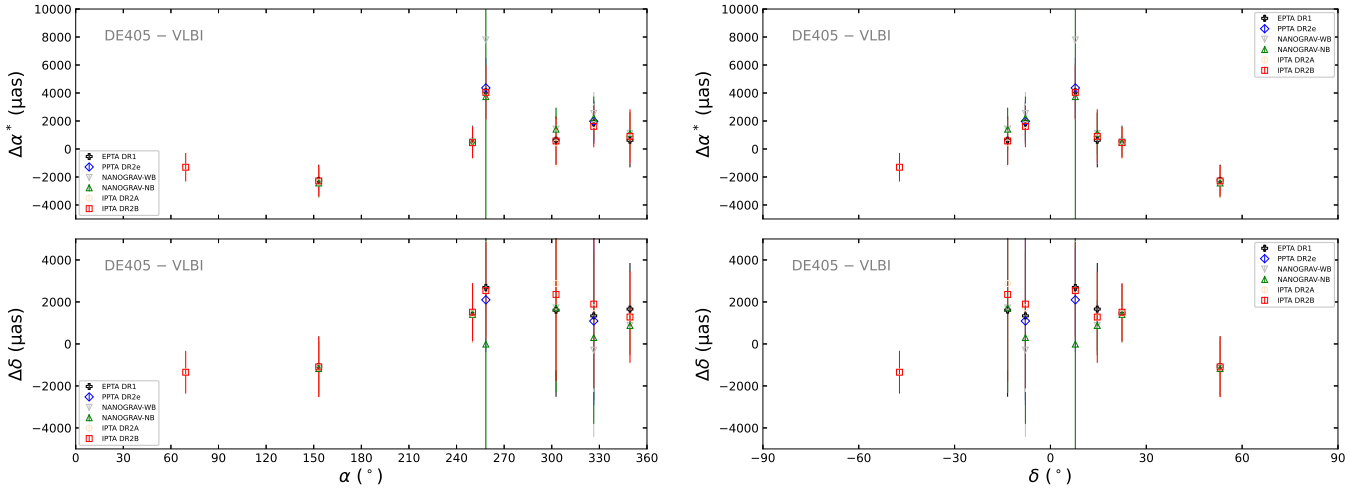

Fig. 13. Offsets of the pulsar timing positions in the DE405 frame with respect to those in the VLBI frame as a function of right ascension (left) and declination (right).

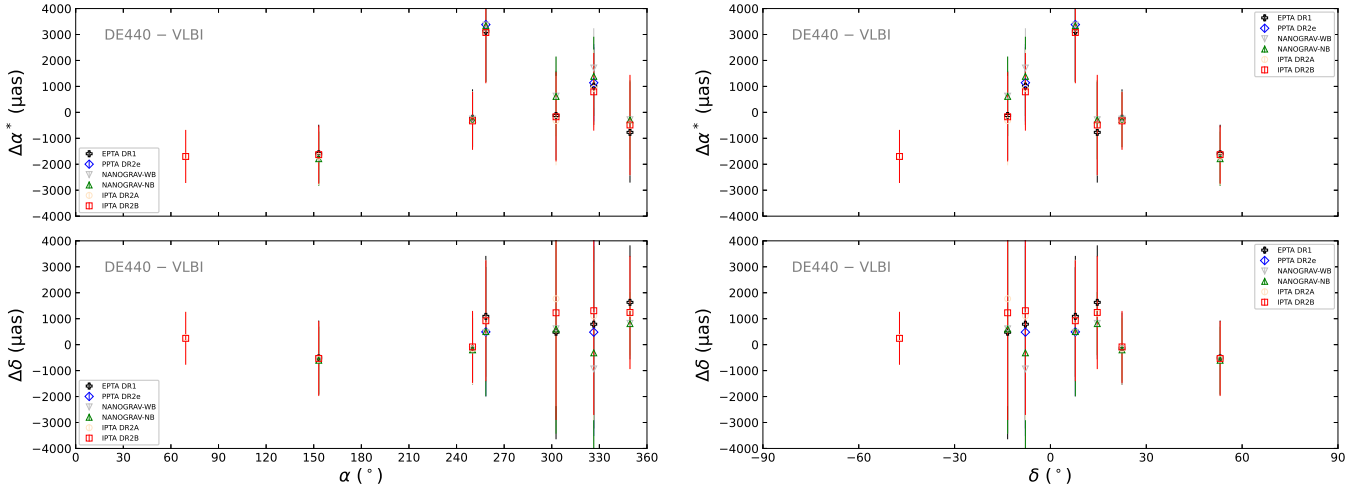

Fig. 14. Offsets of the pulsar timing positions in the DE440 frame with respect to those in the VLBI frame as a function of right ascension (left) and declination (right).

Table 6. Orientation offsets of the planetary ephemeris frames with respect to the VLBI frame.

Ephemeris	R_X (μas)	R_Y (μas)	R_Z (μas)
DE200	−3141(221)	−11806(216)	−14803(189)
DE405	−2478(219)	−372(210)	1200(187)
DE410	−929(212)	−1233(204)	−152(183)
DE421	−904(218)	−820(211)	4(187)
DE430	−1011(220)	−637(216)	431(189)
DE440	−896(221)	−587(217)	292(189)
EPM2011	−1013(221)	−472(217)	668(190)
EPM2015	−1106(221)	−523(217)	619(189)
EPM2017	−1070(218)	−505(212)	529(188)
EPM2021	−971(221)	−600(216)	412(189)
INPOP06c	−893(222)	−882(218)	61(190)
INPOP08a	−655(217)	−429(211)	−683(187)
INPOP10a	−769(217)	−763(211)	311(187)
INPOP10b	−900(221)	−286(216)	534(189)
INPOP10e	−1124(223)	−726(217)	242(190)
INPOP13c	−1002(221)	−732(217)	210(190)
INPOP17a	−1076(221)	−413(217)	281(190)
INPOP19a	−978(221)	−276(217)	130(189)
INPOP21a	−1170(221)	−164(216)	225(189)

Notes. The uncertainties of these estimates given in parentheses were obtained from the least-square fitting and could be underestimated several times.

frame rotation between the DE200 frame and the VLBI frame at J2000.0, plus the propagation of the frame spin.

Since DE403, the tie between all the planetary ephemeris reference frames and the ICRF is achieved through the adjustment of the planetary ephemerides to the VLBI observations of the spacecraft relative to the extragalactic sources. For the orbits of inner planets, this frame tie is dominated by VLBI measurements of Mars-orbiting spacecraft. Therefore, the accuracy of the frame tie between the planetary ephemeris reference frames and the ICRF is on the same level as the accuracy of these VLBI measurements.

The DE405 frame was tied to ICRF1 (Ma et al. 1998) with an uncertainty of ∼1 mas (Standish 1998) based on VLBI observations of the *Magellan* spacecraft in orbit around Venus. Later, in DE410, the frame tie was improved by VLBI points of Mars-orbiting spacecraft (Standish 2003). The improvement of frame-tie from DE405 to DE410 can be easily seen in Table 6, although our estimations suggest larger orientation offsets between these two ephemeris frames and the VLBI frame.

The DE421 frame was tied to the ICRF1 with an accuracy better than 1 mas (Folkner et al. 2009). Fienga et al. (2013) reported that the link between the INPOP10e reference frame and the ICRF was maintained with an accuracy of ∼1 mas over 10 yr. Pitjeva (2013) determined the orientation offset of the EPM2011 frame with respect to the ICRF1, which depended strongly on the time span of the input VLBI observations of various spacecraft. Nevertheless, the frame tie between EPM2011 and ICRF1 is most likely to also be better than 1 mas. Our comparisons between the timing and VLBI solutions agree with these results within the quoted uncertainty.

The DE430 frame was aligned with ICRF2 (Fey et al. 2015) with an accuracy of 0.2 mas (Folkner et al. 2014b; Folkner & Border 2015). Park et al. (2015) also determined the orientation of the DE430 frame relative to the ICRF by using VLBA measurements of Mars with an uncertainty of 0.23 mas. The link accuracy of the INPOP13c frame to ICRF2 was improved to be better than 0.5 mas compared to INPOP10e (Fienga et al. 2014). The EPM2015 and EPM2017 frames were oriented to the ICRF2 with an accuracy better than 0.2 mas at 3 sigma (Pitjeva 2017; Pitjeva & Pitjev 2018). A recent study presented by Deram et al. (2022) used the observations of asteroids in the *Gaia* Data Release 2 (Gaia Collaboration 2018a) to determine the frame rotation between the INPOP19a reference frame and *Gaia*-CRF2 (Gaia Collaboration 2018b). The misalignment between these two reference frames was found to be approximately 0.25 mas; it decreased to a few μas when only very accurate observations of inner planets were considered. Considering that the agreement between *Gaia*-CRF2 and ICRF3 is on the level of 20 μas–30 μas (Gaia Collaboration 2018b; Charlot et al. 2020; Liu et al. 2020), the tie between the INPOP19a frame and ICRF3 should be accurate at 0.25 mas or much better. The average accuracy of the orientation of the inner planet orbits for DE440 tied to ICRF3 is approximately 0.2 mas (Park et al. 2021). For these planetary ephemeris frames, however, we detected a common frame rotation $R_X \simeq -1$ mas that is confident at 4 sigma or higher; this frame rotation would decrease if only an individual PTA data set was used. Therefore, we suspected that the common rotation was likely related to the systematics in the input timing data sets.

Fienga et al. (2011) found a significant rotation of ∼10 mas in the planetary ephemerides with respect to the VLBI frame based on four pulsars with both VLBI and timing astrometric measurements, which diminishes in our results with improved timing and VLBI astrometric data. Therefore, the rotation reported in Fienga et al. (2011) is likely caused by the unmodeled systematics in the input timing or VLBI positions used therein. Wang et al. (2017) studied the rotation between VLBI positions and timing positions using different ephemerides (DE405, DE414, DE421, DE430, DE432, and DE435) for five millisecond pulsars and reported a statistically significant rotation angle of ∼2 mas around the *X*-axis for DE405. Similar results were obtained in our comparison (see Table 6).

The orientation offsets of the DE440, EPM2021, and INPOP21a frames with respect to the VLBI frame range from 0.2 mas to 1.2 mas in an absolute sense. Taking the formal uncertainty of ∼0.2 mas of the rotation parameters and the possible systematics of 0.3 mas–0.6 mas (Sect. 3.3) into consideration, the nonzero orientation offset of the ephemeride frame is approximately 0.4 mas. This deviation is similar to the accuracy of the input VLBI measurements used for constructing the planetary ephemerides (Table 1).

We noted that the formal uncertainty of the frame rotation based on pulsar astrometry was close to those based on the VLBA measurements, even though we used only a small fraction of the sample from the MSPSRπ campaign. More precise frame-tie between the planetary ephemeris frame and the VLBI frame via pulsars could be expected with the increased sample size and reduced systematics in the absolute VLBI positions in the future data release of this campaign.

4.2. Accuracy of state-of-the-art planetary ephemeris reference frames

The orientation offset and global spin of the ephemerides generally decrease with respect to the latest ephemerides in each series (i.e., DE440, EPM2021, and INPOP21a). These results can be expected and validate the improvements in

the error control for the successive ephemerides in the DE, EPM, and INPOP series from the aspect of the pulsar timing astrometry.

According to Standish (2004a), there are three main factors determining the accuracy of an ephemeris, including (i) the correctness and completeness of the equations of motion, (ii) the method and algorithm of integration, and (iii) the input observational data to create the ephemeris. The third factor contributed mainly to the improvements of the ephemerides in the DE series since DE405. Here, we use the INPOP series as an example to discuss the effect of these factors on our results, for which INPOP21a is used as the reference ephemeris. There was no modification in the dynamical modeling of INPOP10a compared with INPOP08, but new observations, especially the normal points deduced from flybys of the MESSENGER spacecraft around Mercury, were used to create INPOP10a (Fienga et al. 2011). This may explain the improvements of 0.4 mas in the orientation of the INPOP10a frame compared with the INPOP08a frame. INPOP10a and INPOP10b were fitted on the same data sample, while the modeling of the asteroid perturbations on planet orbits for INPOP10b was improved and determined with an advanced algorithm (Fienga et al. 2012). Our comparison suggests that the orientation offset of the INPOP10b frame is reduced by 0.4 mas in the Y-axis compared to the INPOP10a frame, which can be considered as a contribution from the first two factors.

The orientation agreement was found to be better than 0.15 mas between DE440 and EPM2021 frames and 0.40 mas between DE440 and INPOP21a frames (Sect. 3.1). In addition, the discrepancy of orientation between the ephemerides frames and VLBI frame was estimated to be ∼0.4 mas (Sect. 4.1.2). From these results, we conclude that the orientation of the state-of-art planetary ephemeris frames is accurate at 0.4 mas. The relative spin is approximately 2 μas yr^{-1} between DE440 and EPM2021 and 5 μas yr^{-1} between DE440 and INPOP21a, leading to the conclusion that the nonrotation of the planetary frame is no greater than 5 μas yr^{-1}. In addition, there is no significant dipolar deformation in the planetary frames at the level of 1 μas in the position and 0.1 μas yr^{-1} in the proper motion.

5. Conclusions

In this work, we utilized the up-to-date pulsar timing observations from the data releases of several pulsar timing arrays and astrometric VLBI measurements for pulsars to investigate the systematics in the planetary ephemeris reference frames. We reported the rotation and glide in the position and proper motion systems of successive editions of the DE series, EPM series, and INPOP series with respect to those of DE440, which is as precise as several μas in position and 0.1 μas yr^{-1} in proper motion. Depending on the sky location, the variations in the pulsar timing position and proper motion due to different choices of planetary ephemerides are on the same order of magnitude as the derived rotation and glide parameters. The orientation offset between the planetary ephemeris frames and VLBI frame is estimated to be approximately 0.4 mas when considering both the formal uncertainty and possible systematics. Our determinations of rotation parameters are improved compared to previous studies thanks to the precise pulsar timing observations of more than 60 millisecond pulsars, which were not available before. Based on the results mentioned above, we conclude that the misalignment of the latest planetary reference frames is no greater than 0.4 mas with a nonrotation of better than 5 μas yr^{-1}.

Acknowledgements. We sincerely thank the referee, Dr. Agnès Fienga, for the constructive comments and useful suggestions, which have greatly improve the work. We wish to thank Prof. Xue-Mei Deng for her critical reading and comments on the first draft. We also thank Dr. Jing Luo for his kind instructions on `PINT`. N. Liu and Z. Zhu were supported by the National Natural Science Foundation of China (NSFC) under grants Nos 11833004 and 12103026. N. Liu was also supported by the China Postdoctoral Science Foundation (Grant Number: 2021M691530) and the Yuxiu Postdoctoral Institute at Nanjing University ("Yuxiu Young Scholars Program"). J. Antoniadis was supported by the Stavros Niarchos Foundation (SNF) and the Hellenic Foundation for Research and Innovation (H.F.R.I.) under the 2nd Call of "Science and Society" Action Always strive for excellence – "Theodoros Papazoglou" (Project Number: 01431). This research also made use of Numpy (van der Walt et al. 2011), IPython (Perez & Granger 2007), Astropy (`http://www.astropy.org`; Astropy Collaboration 2018), the Python 2D plotting library Matplotlib (Hunter 2007), and NASA's Astrophysics Data System. All the results shown in this work are also presented in a series of PYTHON JUPYTER NOTEBOOKS posted and publicly accessible online (`https://git.nju.edu.cn/neo/pulsar-ephem-crf`).

References

Alam, M. F., Arzoumanian, Z., Baker, P. T., et al. 2021a, ApJS, 252, 4
Alam, M. F., Arzoumanian, Z., Baker, P. T., et al. 2021b, ApJS, 252, 5
Antoniadis, J. 2021, MNRAS, 501, 1116
Astropy Collaboration (Price-Whelan, A. M., et al.) 2018, AJ, 156, 123
Bartel, N., Chandler, J. F., Ratner, M. I., et al. 1996, AJ, 112, 1690
Bernus, L., Minazzoli, O., Fienga, A., et al. 2019, Phys. Rev. Lett., 123, 161103
Bernus, L., Minazzoli, O., Fienga, A., et al. 2020, Phys. Rev. D, 102, 021501
Bernus, L., Minazzoli, O., Fienga, A., et al. 2022, Phys. Rev. D, 105, 044057
Burke-Spolaor, S., Taylor, S. R., Charisi, M., et al. 2019, A&ARv, 27, 5
Caballero, R. N., Guo, Y. J., Lee, K. J., et al. 2018, MNRAS, 481, 5501
Charlot, P., Jacobs, C. S., Gordon, D., et al. 2020, A&A, 644, A159
Chatterjee, S., Brisken, W. F., Vlemmings, W. H. T., et al. 2009, ApJ, 698, 250
Chen, S., Caballero, R. N., Guo, Y. J., et al. 2021, MNRAS, 508, 4970
Deller, A. T., Tingay, S. J., Bailes, M., & Reynolds, J. E. 2009, ApJ, 701, 1243
Deller, A. T., Goss, W. M., Brisken, W. F., et al. 2019, ApJ, 875, 100
Deng, X.-M., Fan, M., & Xie, Y. 2014, Chinese Astron. Astrophys., 38, 330
Deram, P., Fienga, A., Verma, A. K., Gastineau, M., & Laskar, J. 2022, Celest. Mech. Dyn. Astron., 134, 32
Desvignes, G., Caballero, R. N., Lentati, L., et al. 2016, MNRAS, 458, 3341
Ding, H., Deller, A. T., Freire, P., et al. 2020, ApJ, 896, 85
Feissel, M., & Mignard, F. 1998, A&A, 331, L33
Fey, A. L., Gordon, D., Jacobs, C. S., et al. 2015, AJ, 150, 58
Fienga, A., Manche, H., Laskar, J., & Gastineau, M. 2008, A&A, 477, 315
Fienga, A., Laskar, J., Morley, T., et al. 2009, A&A, 507, 1675
Fienga, A., Laskar, J., Kuchynka, P., et al. 2011, Celest. Mech. Dyn. Astron., 111, 363
Fienga, A., Laskar, J., Verma, A., et al. 2012, Complementary version of INPOP planetary ephemerides, INPOP10b, online document available at `https://www.imcce.fr/content/medias/recherche/equipes/asd/inpop/inpop10b.pdf`
Fienga, A., Manche, H., Laskar, J., Gastineau, M., & Verma, A. 2013, arXiv e-prints [arXiv:1301.1510]
Fienga, A., Manche, H., Laskar, J., Gastineau, M., & Verma, A. 2014, arXiv e-prints [arXiv:1405.0484]
Fienga, A., Deram, P., Viswanathan, V., et al. 2019, Notes Scientifiques et Techniques de l'Institut de Mécanique Céleste (Paris: IMCCE), 109
Fienga, A., Avdellidou, C., & Hanuš, J. 2020a, MNRAS, 492, 589
Fienga, A., Di Ruscio, A., Bernus, L., et al. 2020b, A&A, 640, A6
Fienga, A., Deram, P., Di Ruscio, A., et al. 2021, Notes Scientifiques et Techniques de l'Institut de Mécanique Céleste (Paris: IMCCE), 110
Fienga, A., Bigot, L., Mary, D., et al. 2022, IAU Symp., 364, 31
Folkner, W. M., & Border, J. S. 2015, Highlights Astron., 16, 219
Folkner, W., Kroger, P., & Iijima, B. 1993, JPL Interoffice memorandum, 335, 1
Folkner, W., Border, J., & Iijima, B. 1994a, JPL Interoffice Memorandum, 335, 94
Folkner, W. M., Charlot, P., Finger, M. H., et al. 1994b, A&A, 287, 279
Folkner, W., Kroger, P., Iijima, B., & Border, J. 1994c, JPL Interoffice Memorandum, 335, 94
Folkner, W. M., Standish, E. M., J., Williams, J. G., & Boggs, D. H. 2007, JPL Interoffice Memorandum, 43R-07-005, 1
Folkner, W. M., Williams, J. G., & Boggs, D. H. 2009, Interplanet. Netw. Progr. Rep., 42-178, 1
Folkner, W. M., Williams, J. G., Boggs, D. H., Park, R. S., & Kuchynka, P. 2014b, Interplanet. Netw. Progr. Rep., 42-196, 1
Gaia Collaboration (Brown, A. G. A., et al.) 2018a, A&A, 616, A1
Gaia Collaboration (Mignard, F., et al.) 2018b, A&A, 616, A14

Gaia Collaboration (Klioner, S. A., et al.) 2021, A&A, 649, A9
Gaia Collaboration (Klioner, S. A., et al.) 2022 A&A, 667, A148
Gaia Collaboration (Vallenari, A., et al.) 2023, A&A, 674, A1
Hobbs, G. B., Edwards, R. T., & Manchester, R. N. 2006, MNRAS, 369, 655
Hotan, A. W., Bailes, M., & Ord, S. M. 2006, MNRAS, 369, 1502
Hunter, J. D. 2007, Comput. Sci. Eng., 9, 90
Jones, D. L., Fomalont, E., Dhawan, V., et al. 2011, AJ, 141, 29
Jones, D. L., Folkner, W. M., Jacobson, R. A., et al. 2015, AJ, 149, 28
Jones, D. L., Folkner, W. M., Jacobson, R. A., et al. 2020, AJ, 159, 72
Jones, D., Folkner, W., Park, R., & Dhawan, V. 2021, AAS Meet. Abstr., 53, 142.05
Kaspi, V. M., Taylor, J. H., & Ryba, M. F. 1994, ApJ, 428, 713
Liu, J. C., & Capitaine, N. 2017, A&A, 597, A83
Liu, N., Lambert, S. B., Zhu, Z., & Liu, J. C. 2020, A&A, 634, A28
Liu, N., Zhu, Z., Antoniadis, J., et al. 2023, A&A, 670, A173
Luo, J., Ransom, S., Demorest, P., et al. 2021, ApJ, 911, 45
Ma, C., Arias, E. F., Eubanks, T. M., et al. 1998, AJ, 116, 516
Matthews, A. M., Nice, D. J., Fonseca, E., et al. 2016, ApJ, 818, 92
Mignard, F., & Klioner, S. 2012, A&A, 547, A59
Park, R. S., Folkner, W. M., Jones, D. L., et al. 2015, AJ, 150, 121
Park, R. S., Folkner, W. M., Williams, J. G., & Boggs, D. H. 2021, AJ, 161, 105
Perera, B. B. P., DeCesar, M. E., Demorest, P. B., et al. 2019, MNRAS, 490, 4666
Perez, F., & Granger, B. E. 2007, Comput. Sci. Eng., 9, 21
Pitjeva, E. V. 2005, IAU Colloq., 196, 230
Pitjeva, E. V. 2013, Solar Syst. Res., 47, 386
Pitjeva, E. V. 2017, Trans. IAA RAS, 10
Pitjeva, E. V., & Pitjev, N. P. 2013, MNRAS, 432, 3431
Pitjeva, E. V., & Pitjev, N. P. 2018, Celest. Mech. Dyn. Astron., 130, 57
Pitjeva, E. V., Pitjev, N. P., Pavlov, D. A., & Turygin, C. C. 2021, A&A, 647, A141
Pitjeva, E., Pavlov, D., Aksim, D., & Kan, M. 2022, IAU Symp., 364, 220
Reardon, D. J., Hobbs, G., Coles, W., et al. 2016, MNRAS, 455, 1751
Reardon, D. J., Shannon, R. M., Cameron, A. D., et al. 2021, MNRAS, 507, 2137
Splaver, E. M., Nice, D. J., Stairs, I. H., Lommen, A. N., & Backer, D. C. 2005, ApJ, 620, 405
Standish, E. M. J. 1982, A&A, 114, 297
Standish, E. M. J. 1990a, A&A, 233, 252
Standish, E. M. J. 1990b, A&A, 233, 272
Standish, E. M. J. 1998, JPL Interoffice Memorandum, 312.F-98-048, 1
Standish, E. M. J. 2003, JPL Interoffice Memorandum, 312.N-03-009, 1
Standish, E. M. 2004a, A&A, 417, 1165
Standish, E. M. J. 2004b, JPL Interoffice Memorandum, 343R-06-002, 1
Standish, E. M., & Fienga, A. 2002, A&A, 384, 322
Tkachuk, V. V., & Choliy, V. Y. 2013, Adv. Astron. Space Phys., 3, 141
Vallisneri, M., Taylor, S. R., Simon, J., et al. 2020, ApJ, 893, 112
van der Walt, S., Colbert, S. C., & Varoquaux, G. 2011, Comput. Sci. Eng., 13, 22
Verbiest, J. P. W., Bailes, M., van Straten, W., et al. 2008, ApJ, 679, 675
Verma, A. K., Fienga, A., Laskar, J., Manche, H., & Gastineau, M. 2014, A&A, 561, A115
Vigeland, S. J., Deller, A. T., Kaplan, D. L., et al. 2018, ApJ, 855, 122
Viswanathan, V., Fienga, A., Gastineau, M., & Laskar, J. 2017, Notes Scientifiques et Techniques de l'Institut de Mécanique Céleste (Paris: IMCCE), 108
Wang, J. B., Coles, W. A., Hobbs, G., et al. 2017, MNRAS, 469, 425
Yang, P., Huang, Y., Li, P., et al. 2022, Adv. Space Res., 69, 1060
Yuan, Y., Li, F., Fu, Y., & Chen, J. 2021, A&A, 654, A66

Appendix A: Pulsar timing position differences using different ephemerides

Figures A.1–A.16 present the offsets of the pulsar position from the timing analyses using successive versions of planetary ephemerides from the DE series, EPM series, and INPOP series with respect to those from the timing solution using DE440.

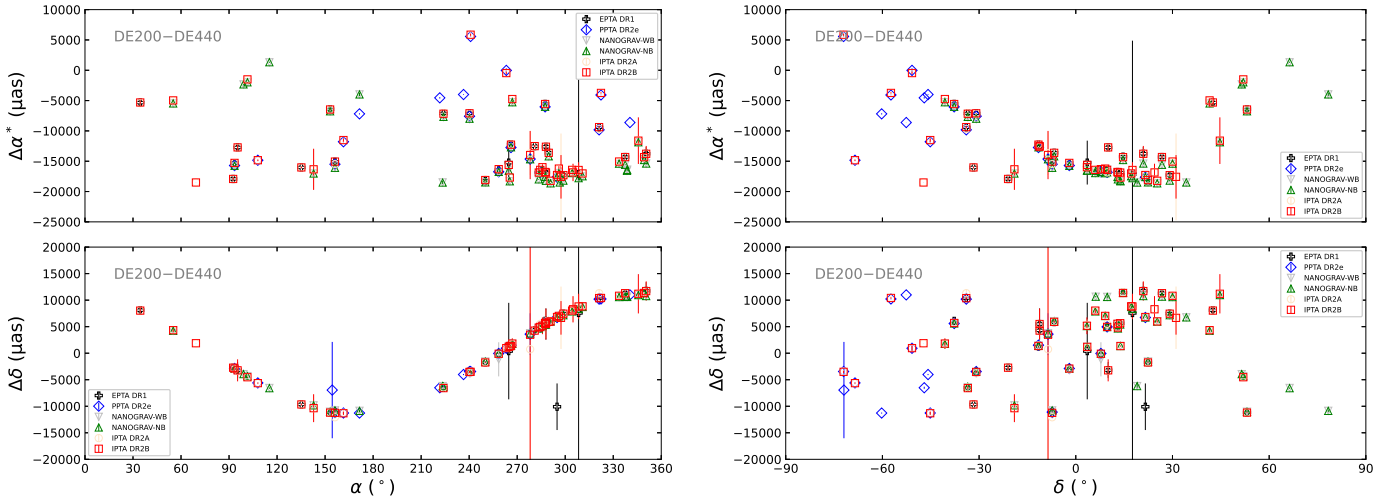

Fig. A.1. Offsets of the pulsar timing positions in the DE200 frame with referred to those in the DE440 frame as a function of the right ascension (left) and declination (right).

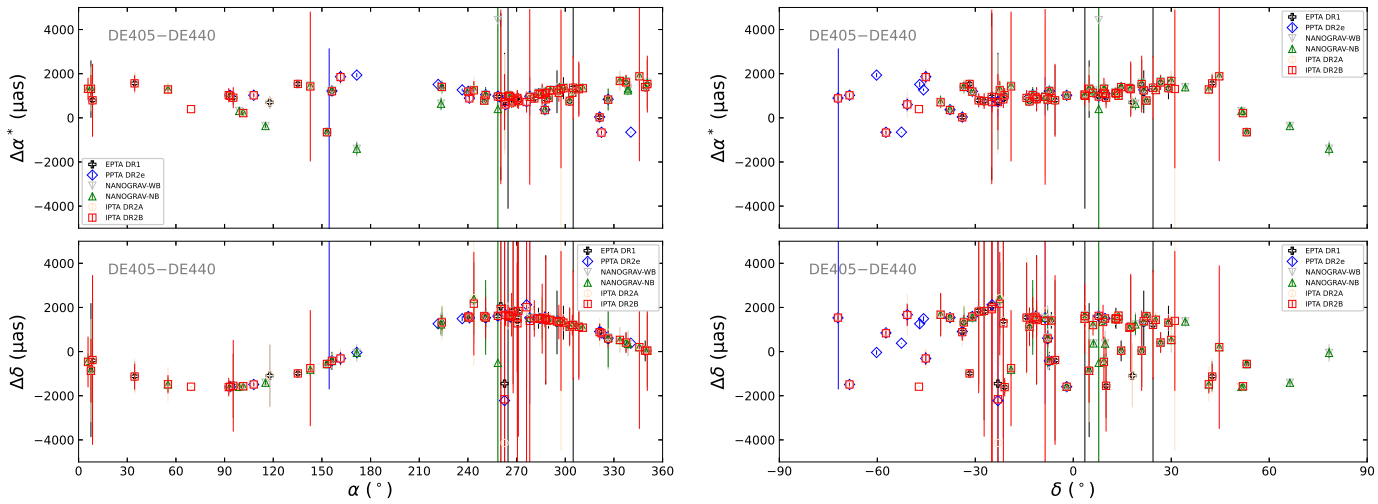

Fig. A.2. Offsets of the pulsar timing positions in the DE405 frame with referred to those in the DE440 frame as a function of the right ascension (left) and declination (right).

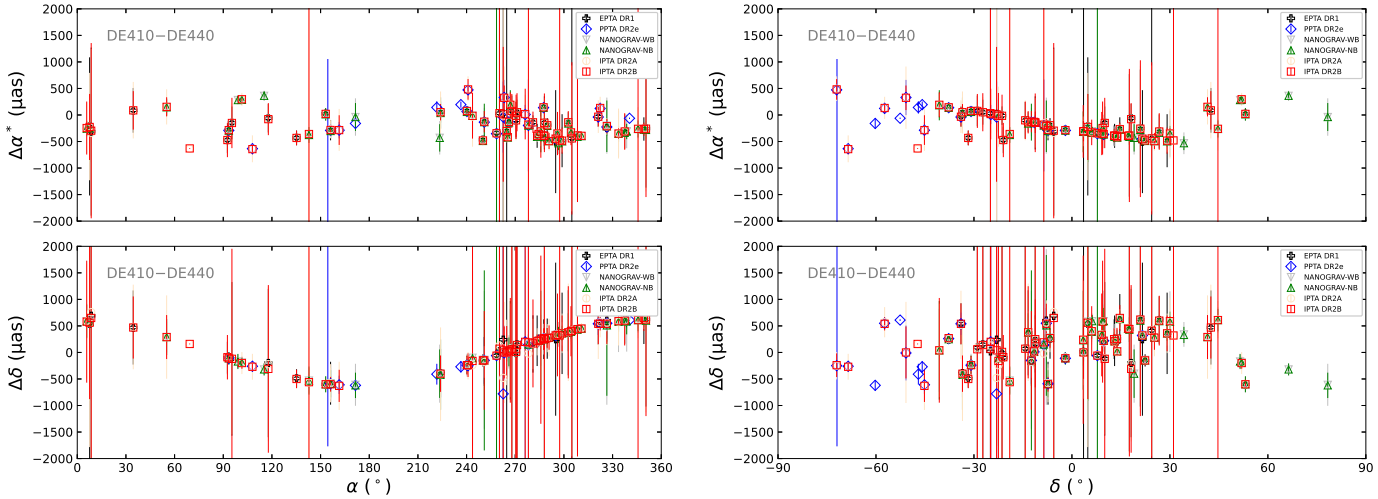

Fig. A.3. Offsets of the pulsar timing positions in the DE410 frame with referred to those in the DE440 frame as a function of the right ascension (left) and declination (right).

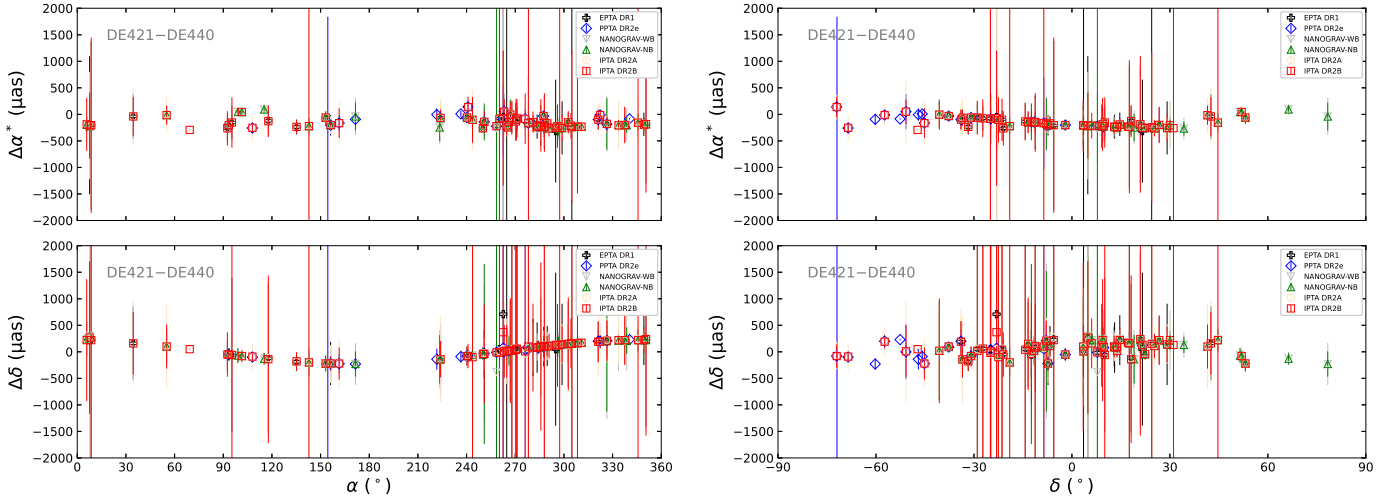

Fig. A.4. Offsets of the pulsar timing positions in the DE421 frame with referred to those in the DE440 frame as a function of the right ascension (left) and declination (right).

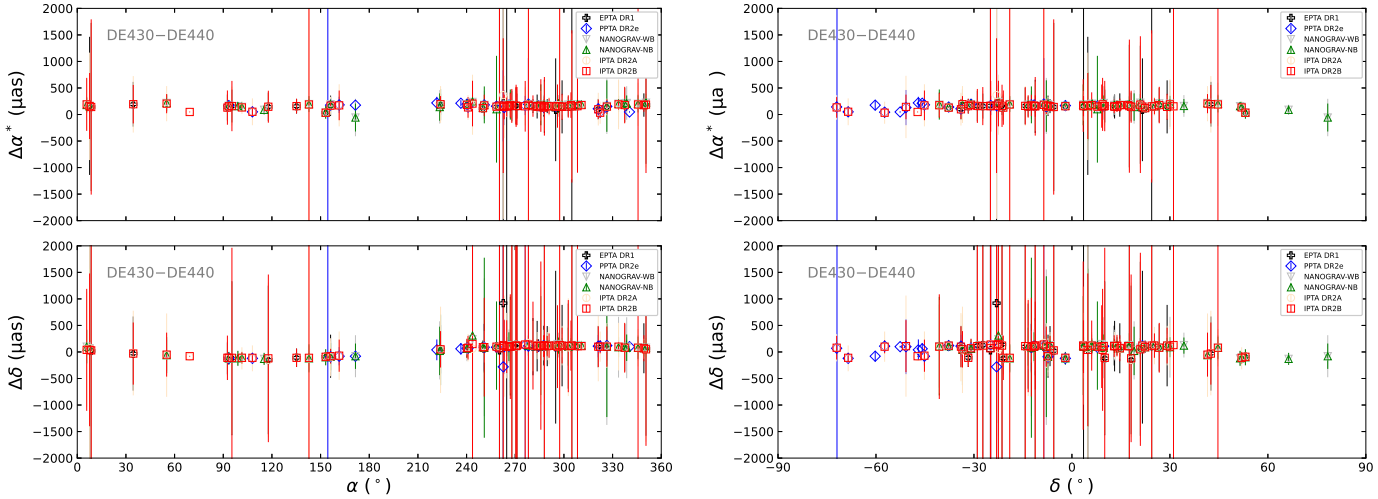

Fig. A.5. Offsets of the pulsar timing positions in the DE430 frame with referred to those in the DE440 frame as a function of the right ascension (left) and declination (right).

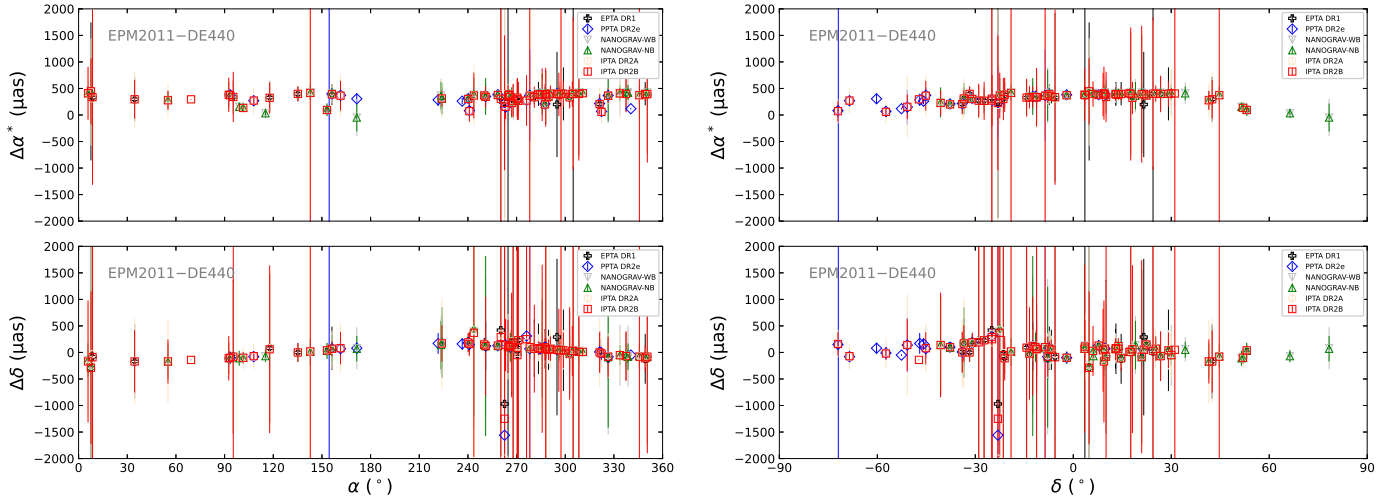

Fig. A.6. Offsets of the pulsar timing positions in the EPM2011 frame with referred to those in the DE440 frame as a function of the right ascension (left) and declination (right).

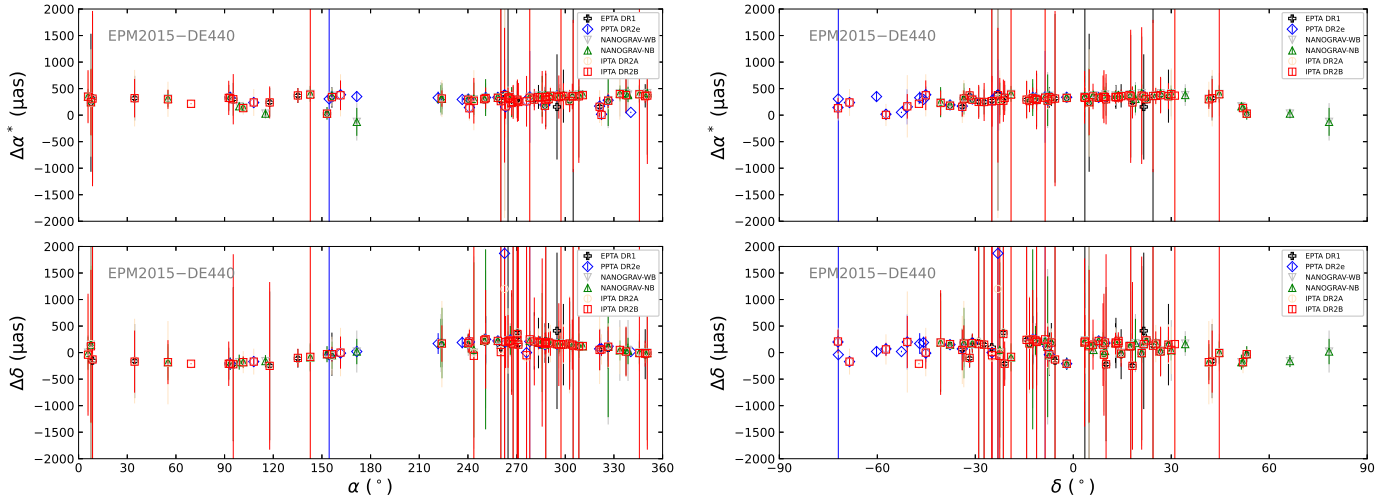

Fig. A.7. Offsets of the pulsar timing positions in the EPM2015 frame with referred to those in the DE440 frame as a function of the right ascension (left) and declination (right).

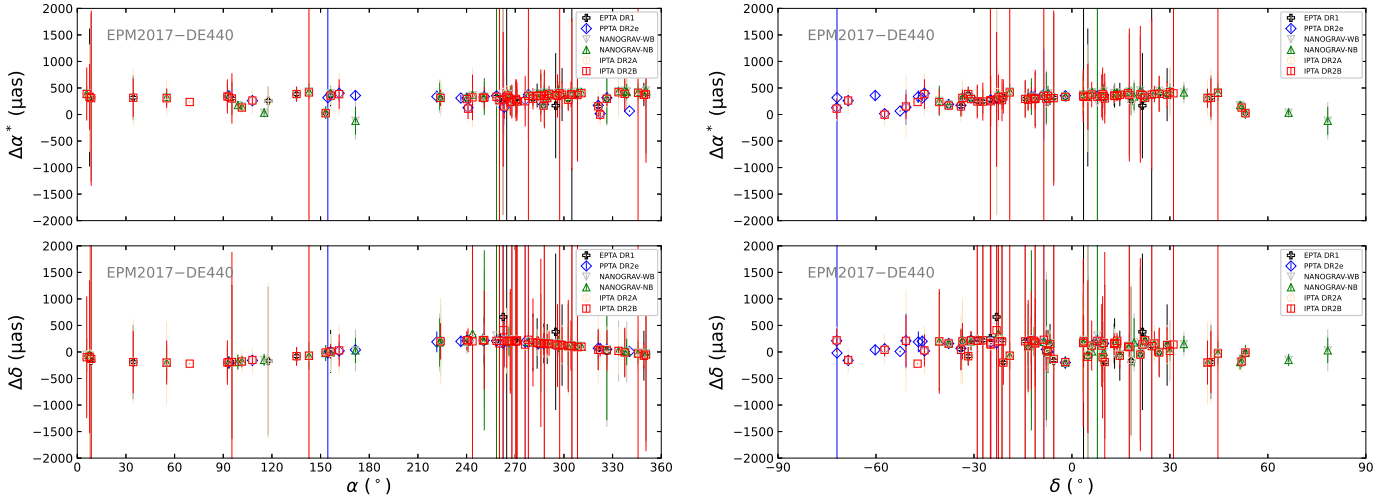

Fig. A.8. Offsets of the pulsar timing positions in the EPM2017 frame with referred to those in the DE440 frame as a function of the right ascension (left) and declination (right).

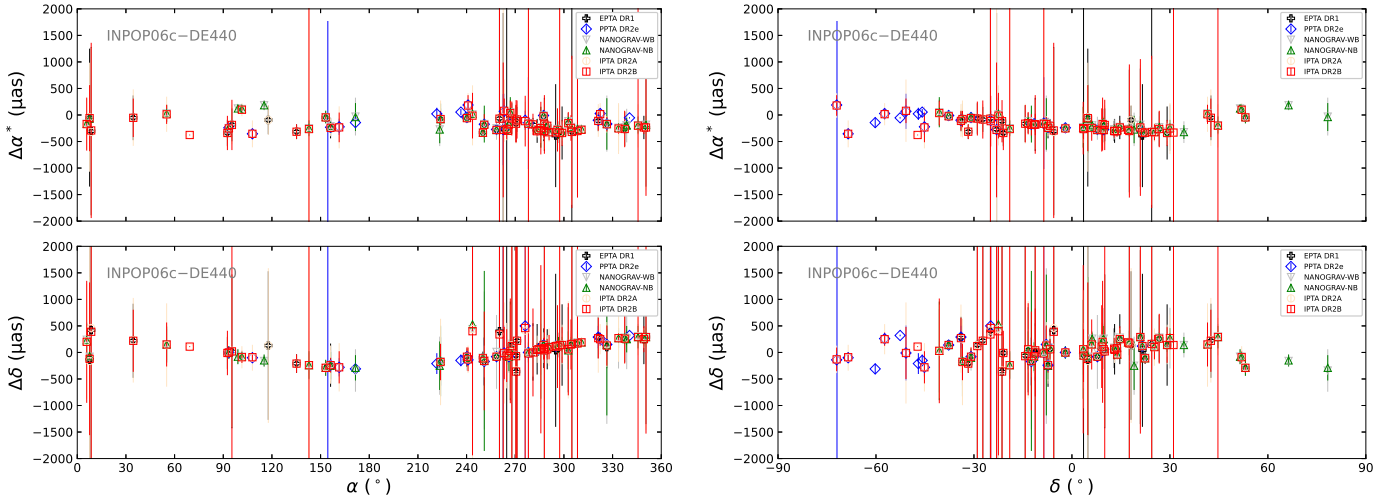

Fig. A.9. Offsets of the pulsar timing positions in the INPOP06c frame with referred to those in the DE440 frame as a function of the right ascension (left) and declination (right).

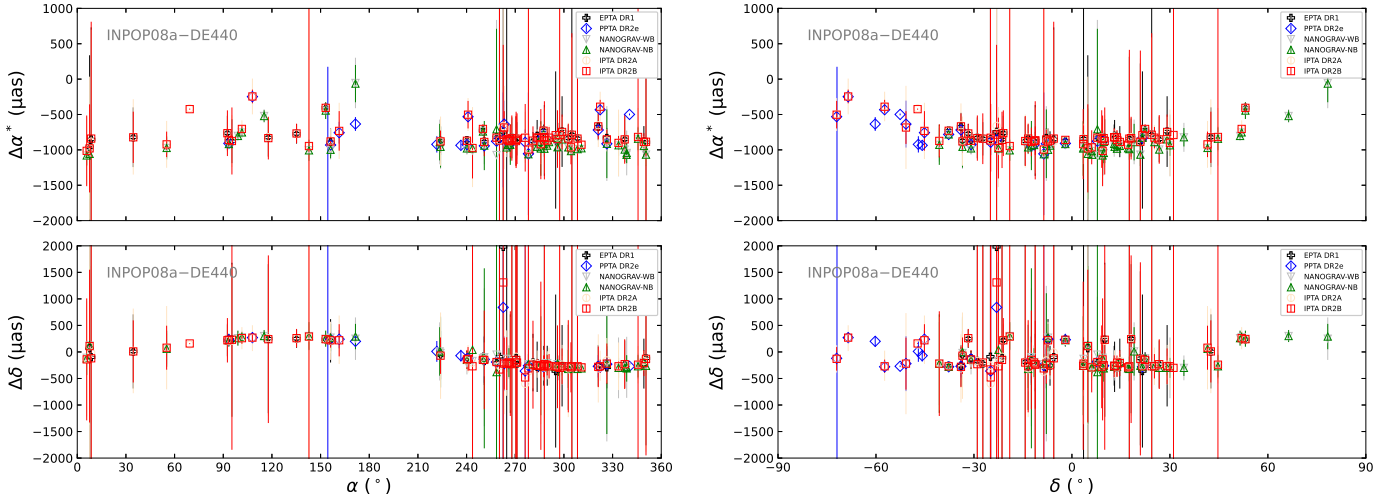

Fig. A.10. Offsets of the pulsar timing positions in the INPOP08a frame with referred to those in the DE440 frame as a function of the right ascension (left) and declination (right).

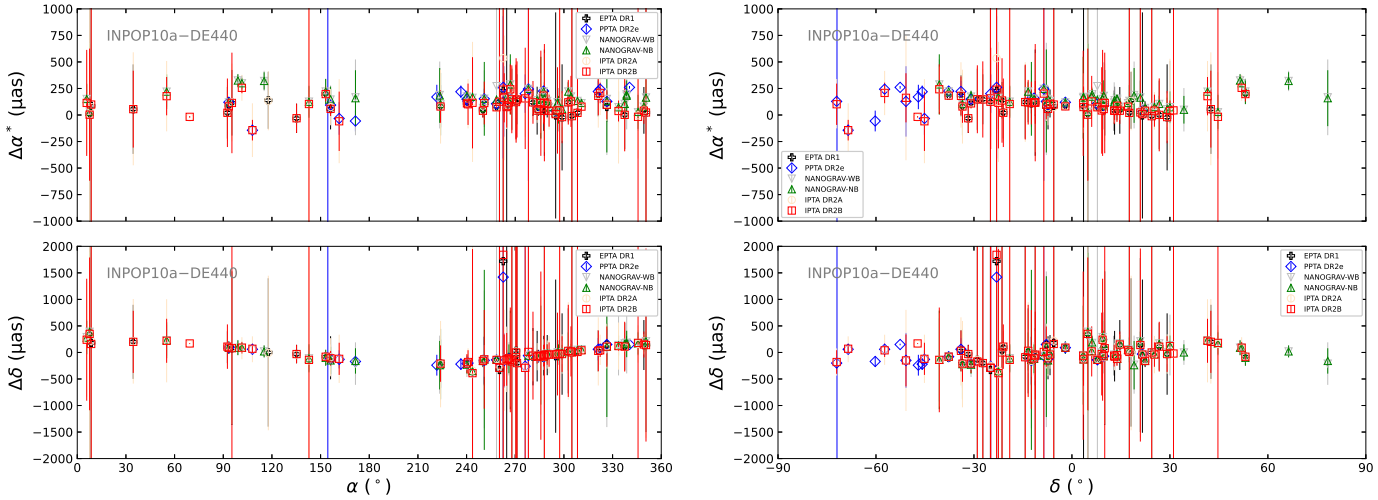

Fig. A.11. Offsets of the pulsar timing positions in the INPOP10a frame with referred to those in the DE440 frame as a function of the right ascension (left) and declination (right).

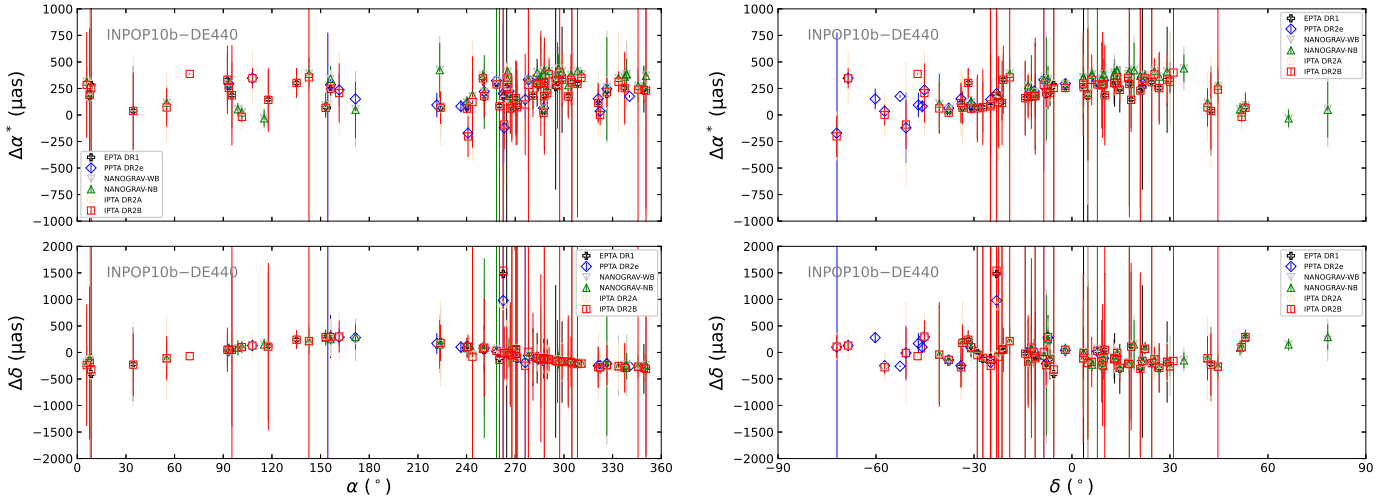

Fig. A.12. Offsets of the pulsar timing positions in the INPOP10b frame with referred to those in the DE440 frame as a function of the right ascension (left) and declination (right).

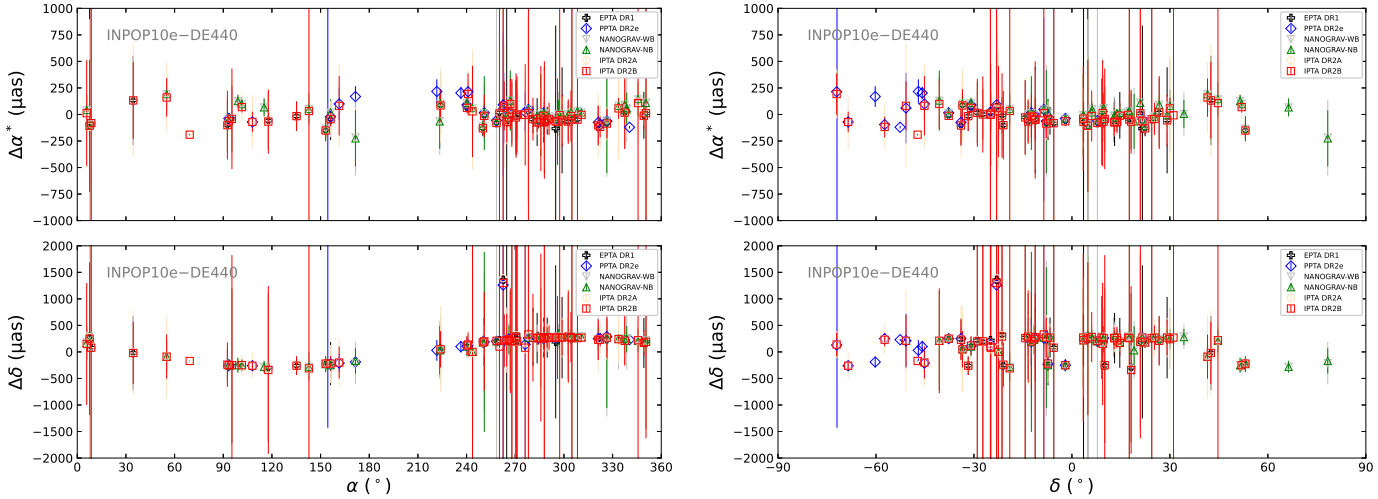

Fig. A.13. Offsets of the pulsar timing positions in the INPOP10e frame with referred to those in the DE440 frame as a function of the right ascension (left) and declination (right).

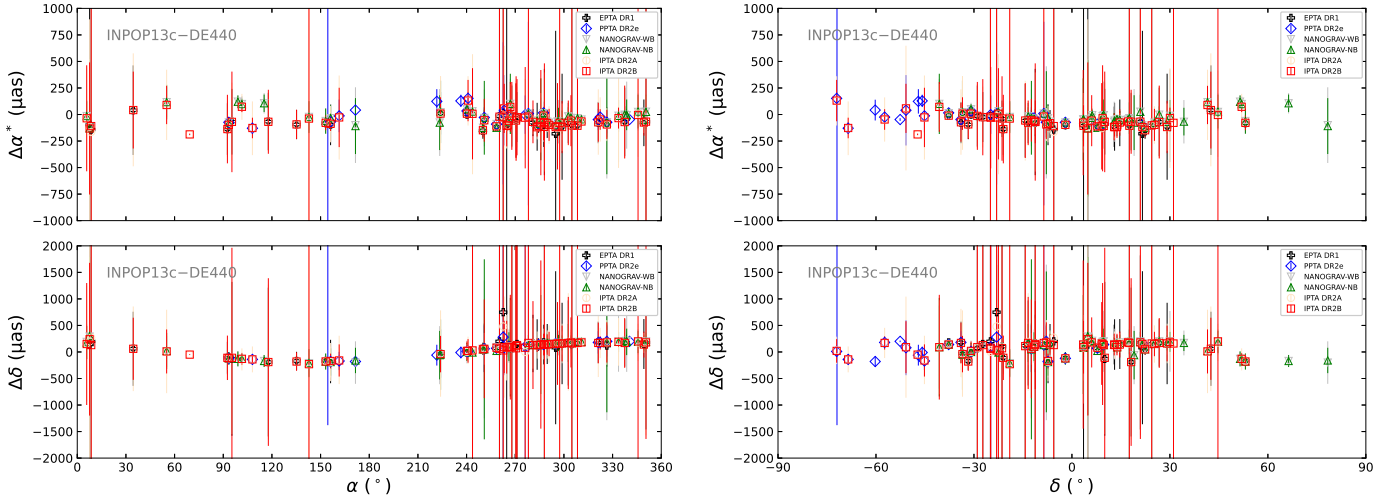

Fig. A.14. Offsets of the pulsar timing positions in the INPOP13c frame with referred to those in the DE440 frame as a function of the right ascension (left) and declination (right).

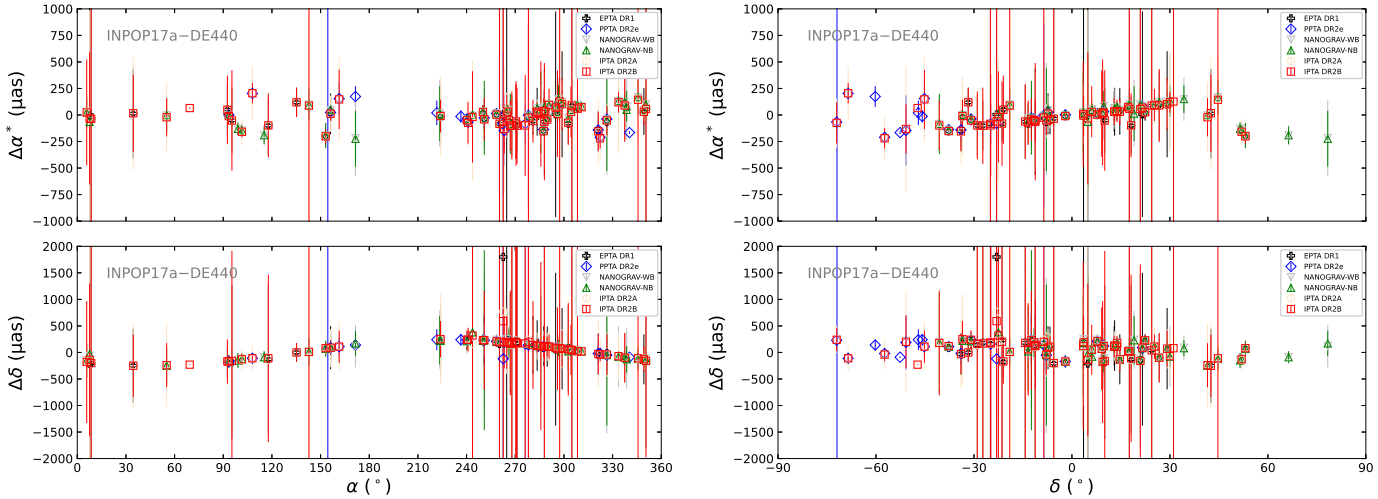

Fig. A.15. Offsets of the pulsar timing positions in the INPOP17a frame with referred to those in the DE440 frame as a function of the right ascension (left) and declination (right).

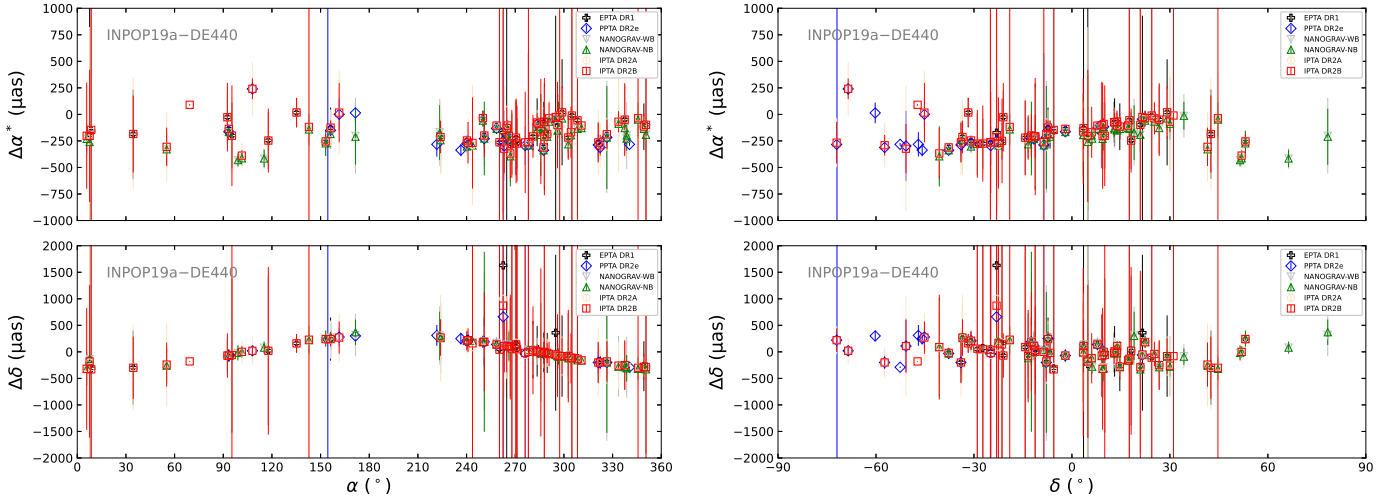

Fig. A.16. Offsets of the pulsar timing positions in the INPOP19a frame with referred to those in the DE440 frame as a function of the right ascension (left) and declination (right).

Appendix B: Pulsar timing proper motion differences using different ephemerides

Figures B.1–B.16 present the offsets of the pulsar proper motion from the timing solutions using successive versions of planetary ephemerides from the DE series, EPM series, and INPOP series with respect to those from the timing solution using DE440.

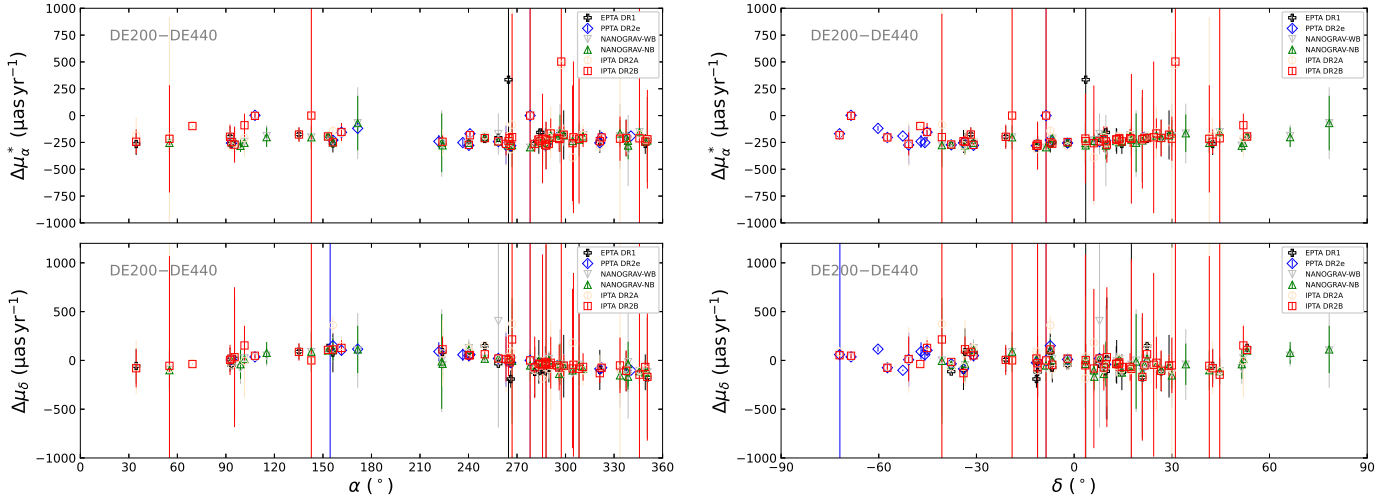

Fig. B.1. Offsets of the pulsar timing proper motions in the DE200 frame with referred to those in the DE440 frame as a function of the right ascension (left) and declination (right).

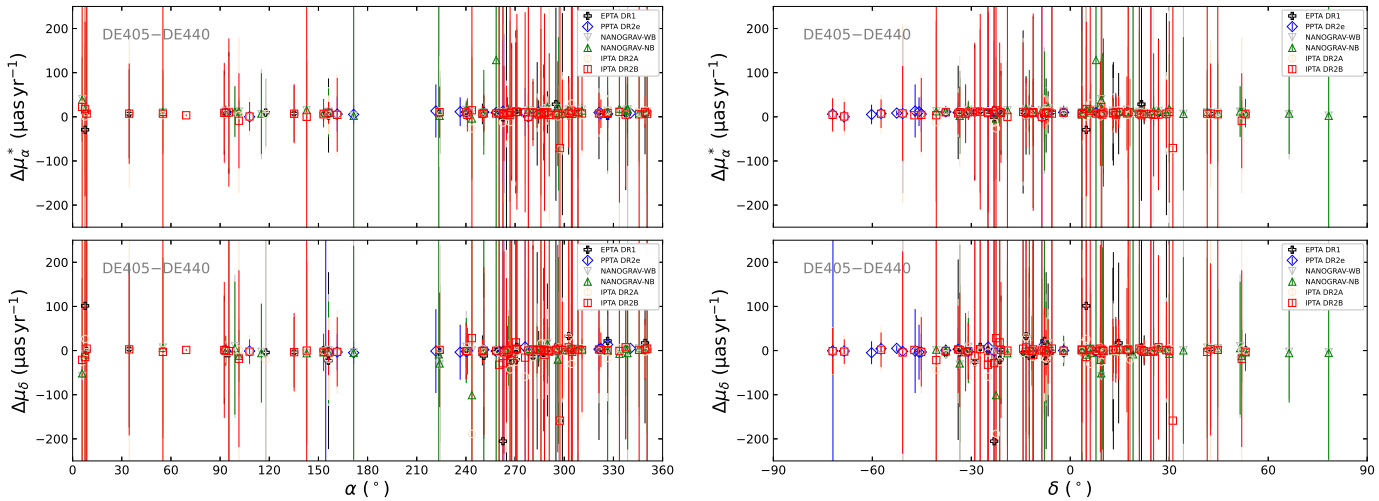

Fig. B.2. Offsets of the pulsar timing proper motions in the DE405 frame with referred to those in the DE440 frame as a function of the right ascension (left) and declination (right).

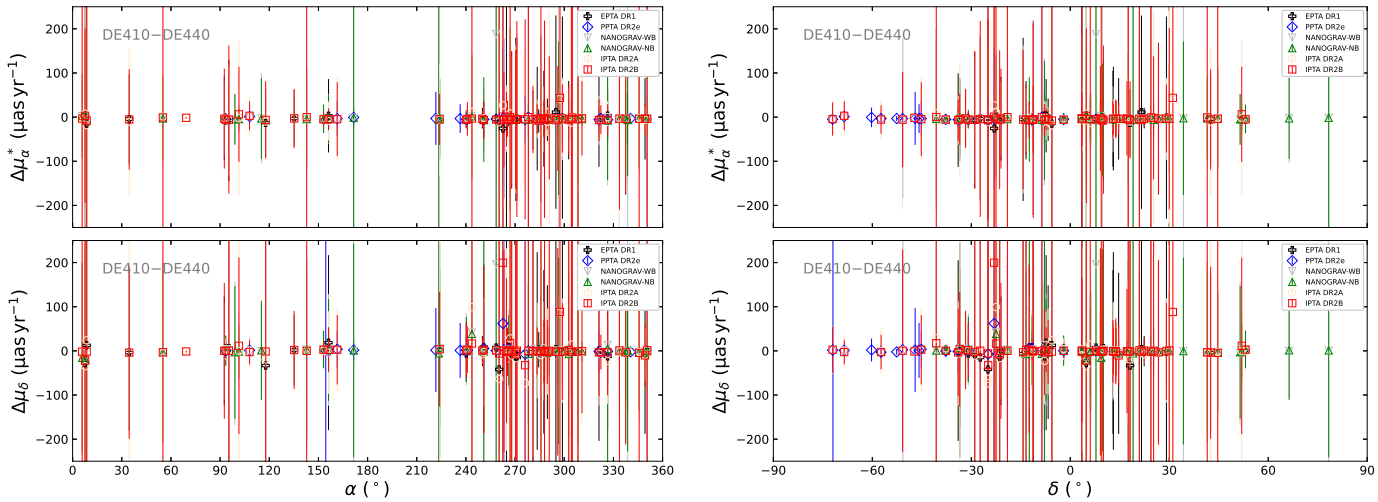

Fig. B.3. Offsets of the pulsar timing proper motions in the DE410 frame with referred to those in the DE440 frame as a function of the right ascension (left) and declination (right).

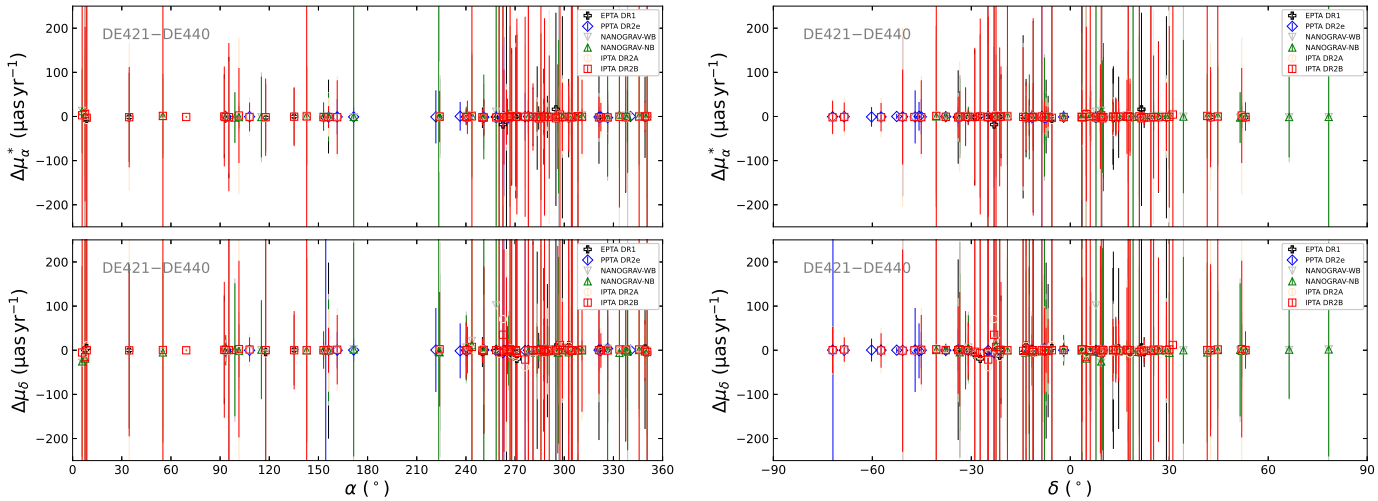

Fig. B.4. Offsets of the pulsar timing proper motions in the DE421 frame with referred to those in the DE440 frame as a function of the right ascension (left) and declination (right).

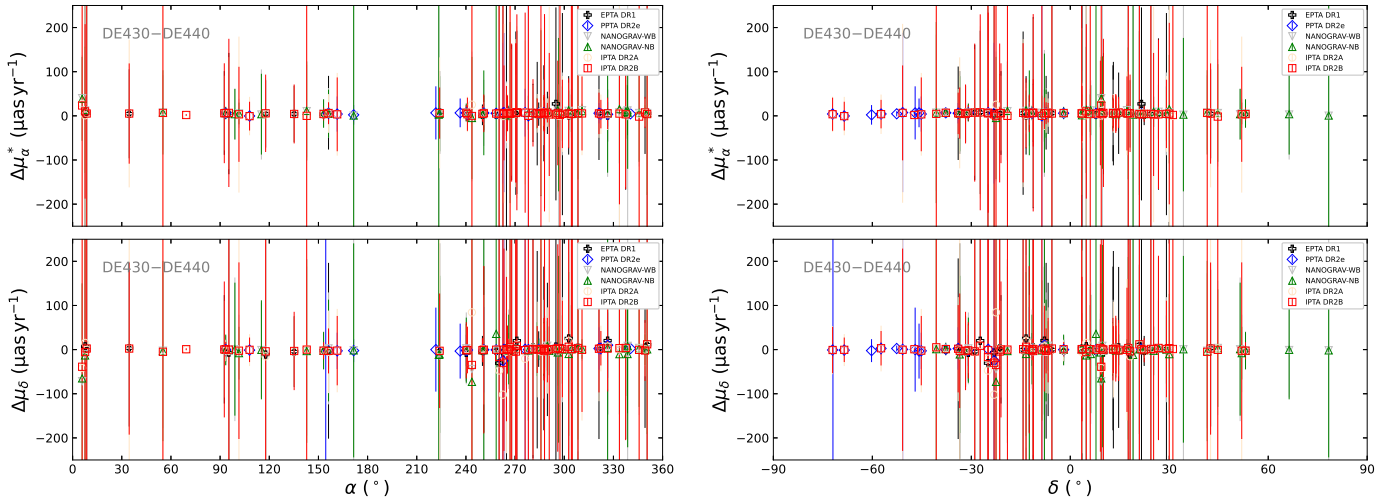

Fig. B.5. Offsets of the pulsar timing proper motions in the DE430 frame with referred to those in the DE440 frame as a function of the right ascension (left) and declination (right).

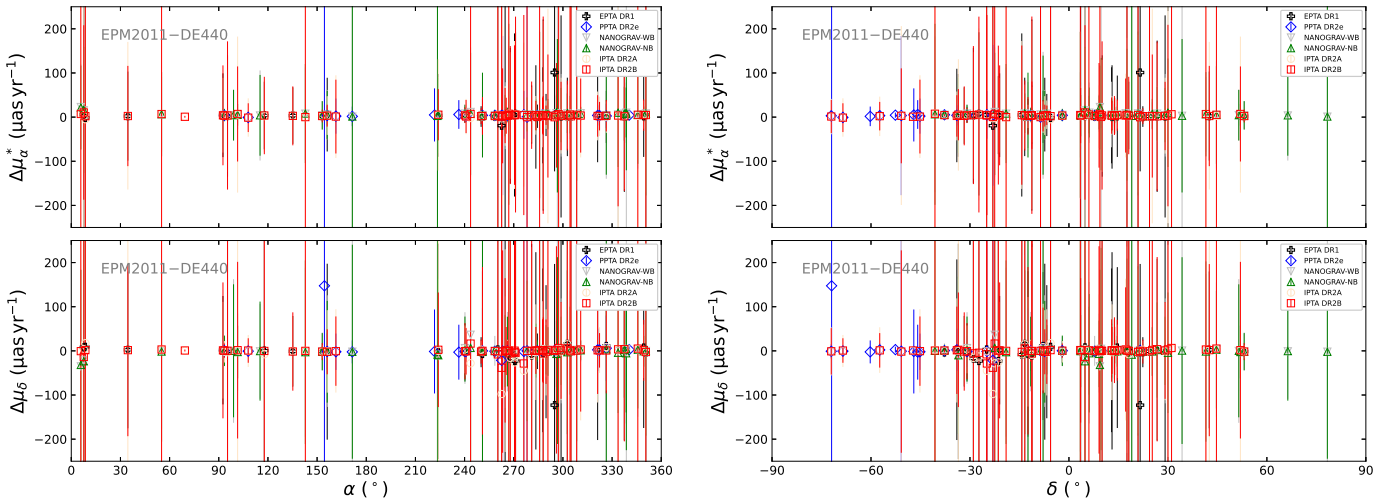

Fig. B.6. Offsets of the pulsar timing proper motions in the EPM2011 frame with referred to those in the DE440 frame as a function of the right ascension (left) and declination (right).

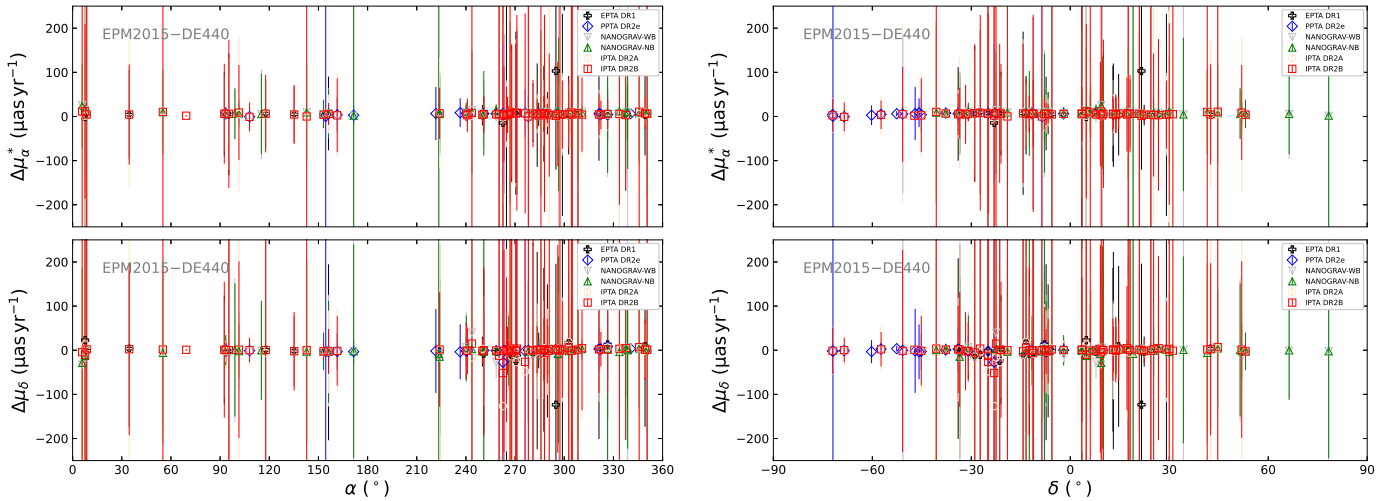

Fig. B.7. Offsets of the pulsar timing proper motions in the EPM2015 frame with referred to those in the DE440 frame as a function of the right ascension (left) and declination (right).

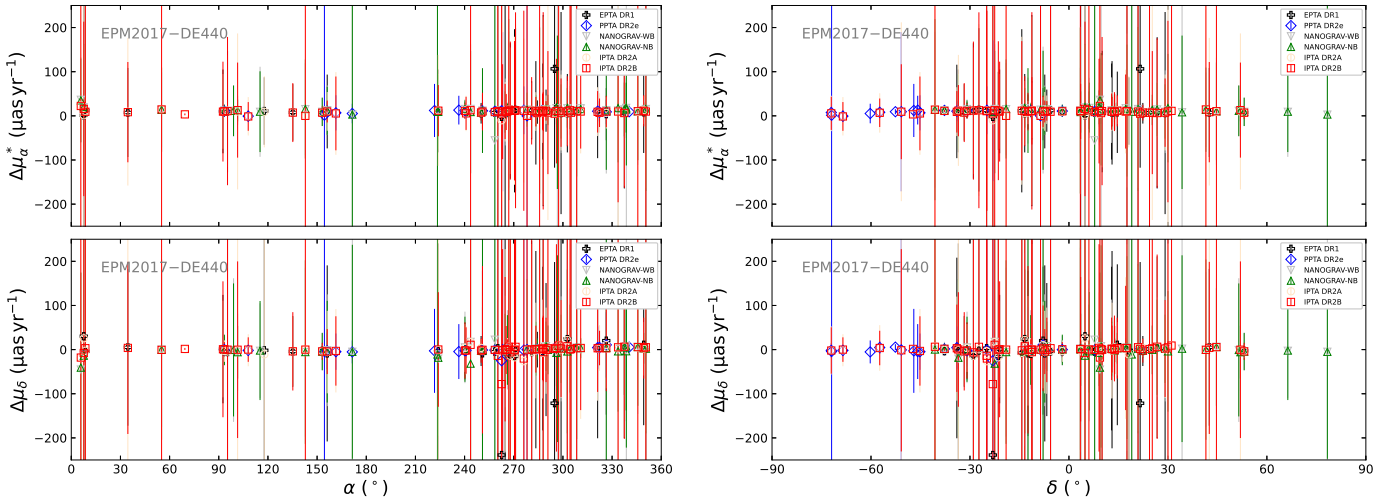

Fig. B.8. Offsets of the pulsar timing proper motions in the EPM2017 frame with referred to those in the DE440 frame as a function of the right ascension (left) and declination (right).

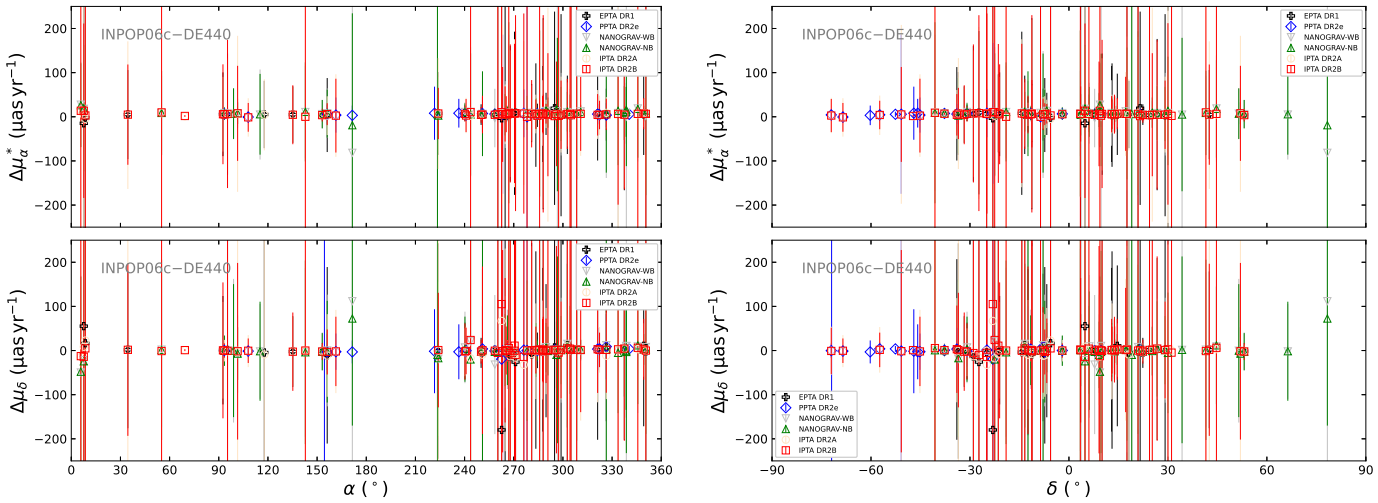

Fig. B.9. Offsets of the pulsar timing proper motions in the INPOP06c frame with referred to those in the DE440 frame as a function of the right ascension (left) and declination (right).

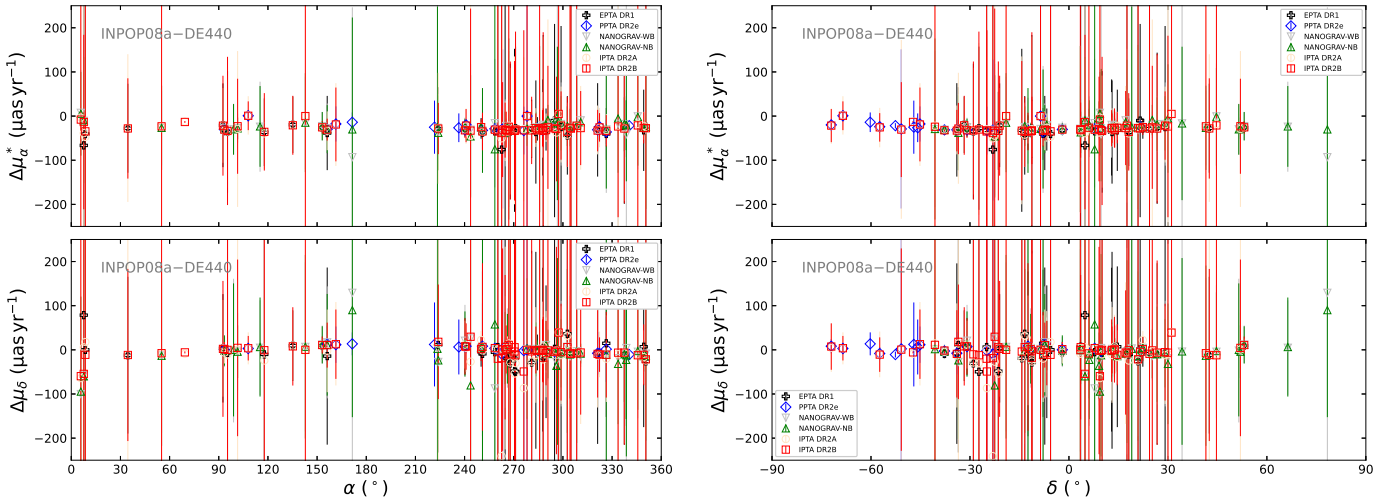

Fig. B.10. Offsets of the pulsar timing proper motions in the INPOP08a frame with referred to those in the DE440 frame as a function of the right ascension (left) and declination (right).

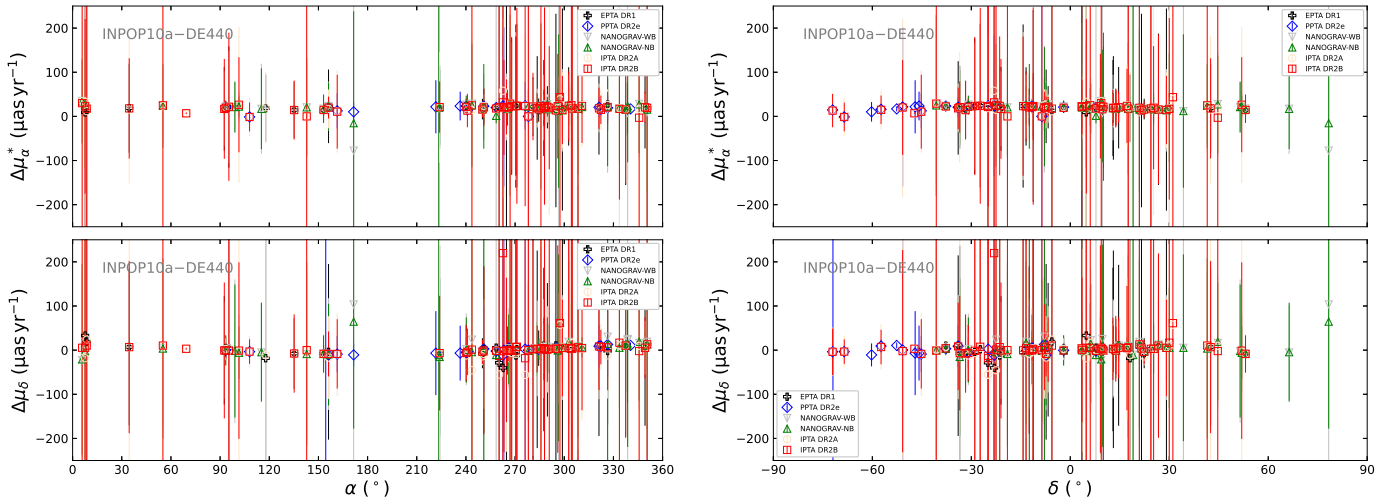

Fig. B.11. Offsets of the pulsar timing proper motions in the INPOP10a frame with referred to those in the DE440 frame as a function of the right ascension (left) and declination (right).

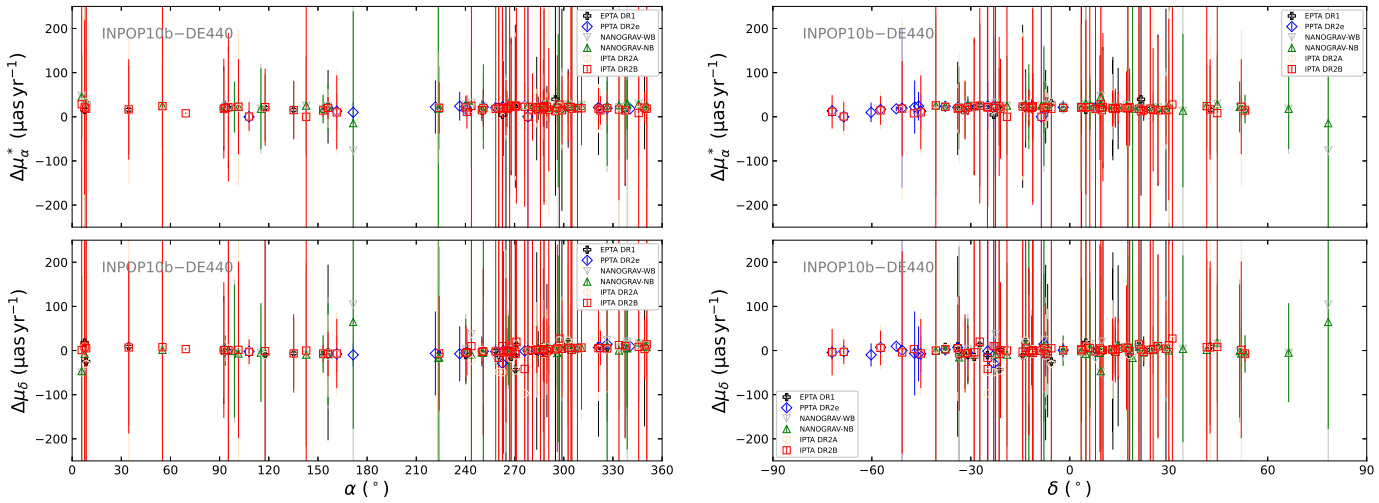

Fig. B.12. Offsets of the pulsar timing proper motions in the INPOP10b frame with referred to those in the DE440 frame as a function of the right ascension (left) and declination (right).

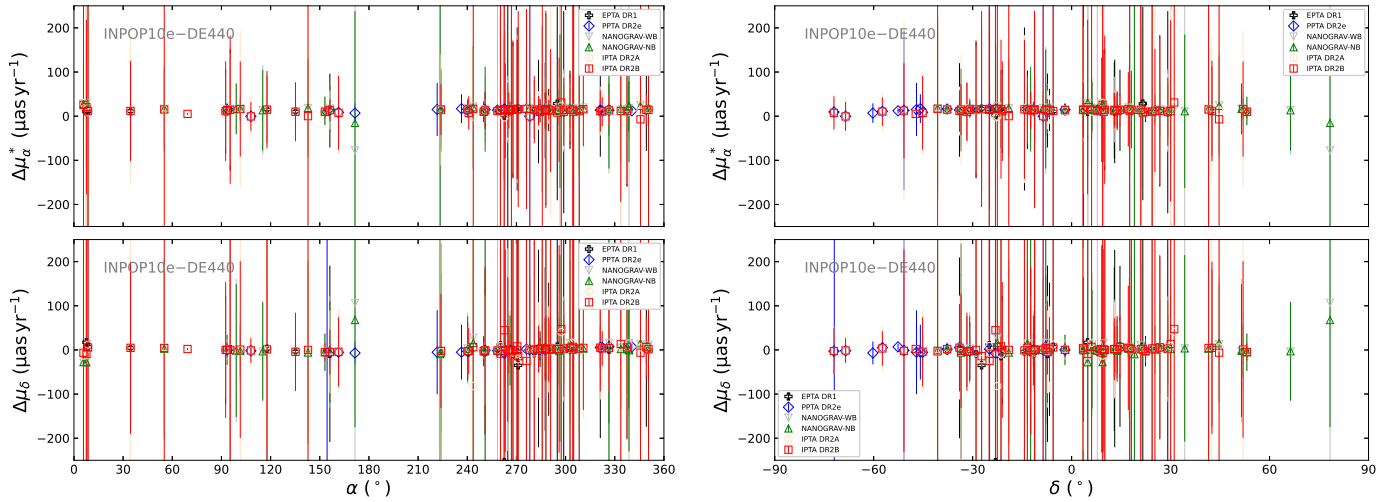

Fig. B.13. Offsets of the pulsar timing proper motions in the INPOP10e frame with referred to those in the DE440 frame as a function of the right ascension (left) and declination (right).

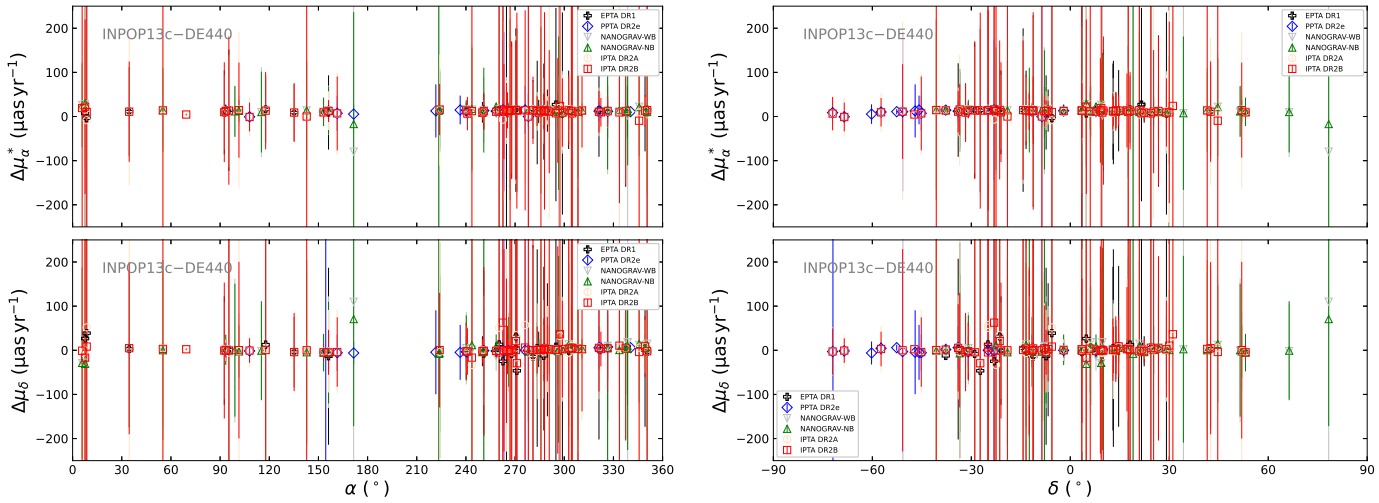

Fig. B.14. Offsets of the pulsar timing proper motions in the INPOP13c frame with referred to those in the DE440 frame as a function of the right ascension (left) and declination (right).

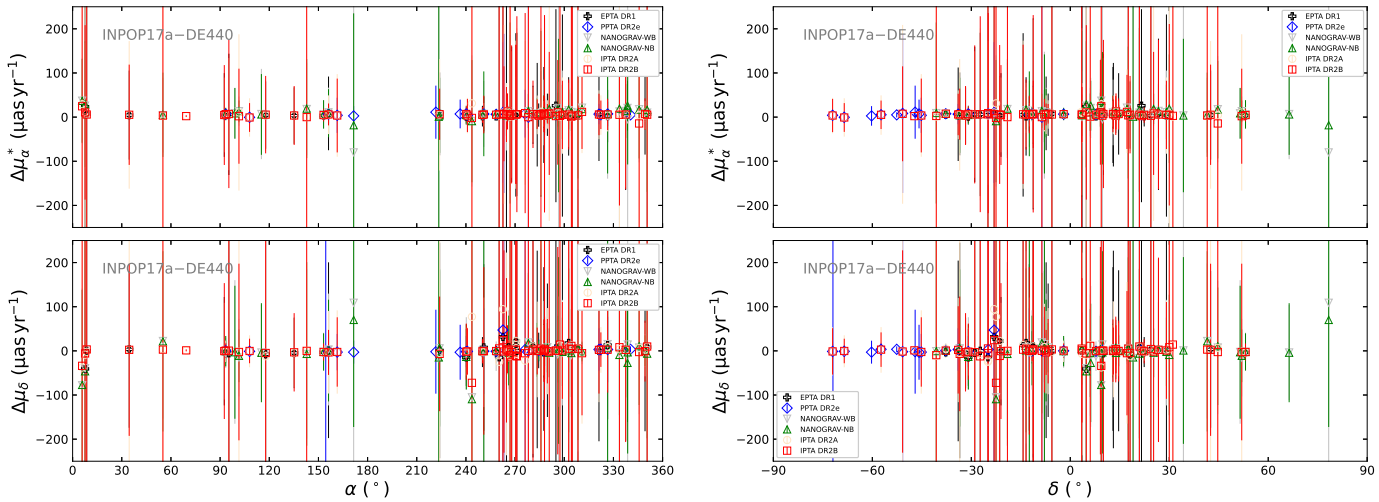

Fig. B.15. Offsets of the pulsar timing proper motions in the INPOP17a frame with referred to those in the DE440 frame as a function of the right ascension (left) and declination (right).

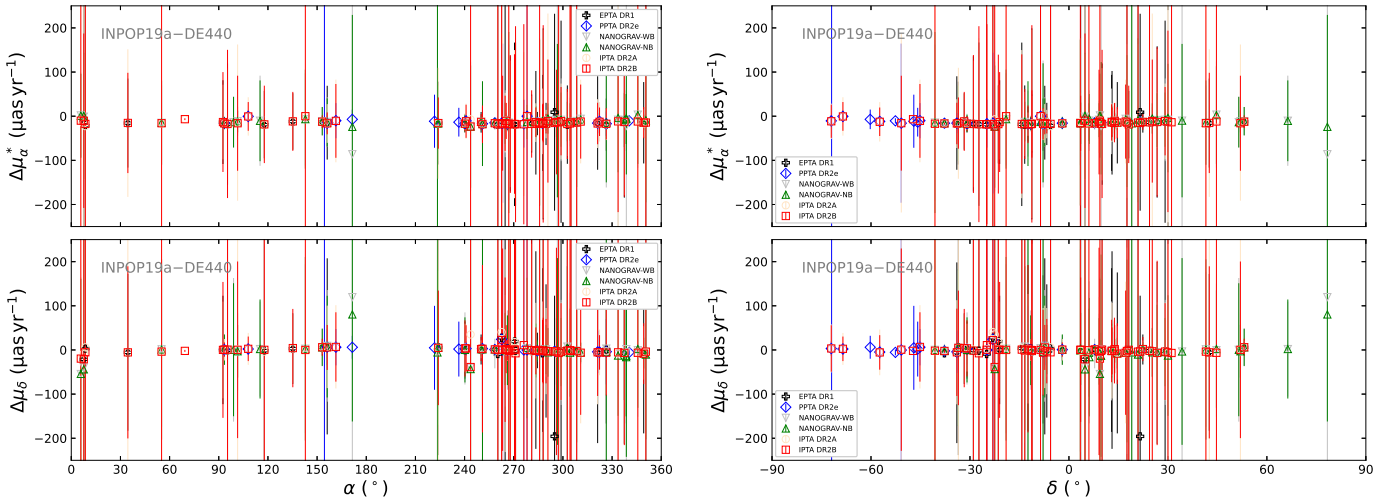

Fig. B.16. Offsets of the pulsar timing proper motions in the INPOP19a frame with referred to those in the DE440 frame as a function of the right ascension (left) and declination (right).